Applied Energy 421 (2026) 128241

Contents lists available at ScienceDirect

Applied Energy

journal homepage: www.elsevier.com/locate/apenergy

Exergoeconomic assessment of the industrial integration of a thermochemical energy storage system with adaptive turbomachinery

J.M. Guisado [a,*], C. Ortiz [c], J.A. Becerra [a,b], A. Marques-Valderrama [a], R. Chacartegui [a,b]

[a] Energy Engineering Department, University of Seville, 41092 Seville, Spain
[b] Laboratory of Engineering for Energy and Environmental Sustainability, University of Seville, 41092 Seville, Spain
[c] Materials and Sustainability Group, Department of Engineering, Universidad Loyola Andalucía, 41704 Seville, Spain

HIGHLIGHTS

- A realistic study of storage system integration under off-design conditions.
- Challenges related to the industrial implementation of turbomachinery-based systems.
- Strategies for operating turbomachinery under off-design conditions.
- Optimization of the modular thermochemical storage system according to industrial demand.

ARTICLE INFO

Keywords:
Storage system
Industrial integration
Thermochemical
Off-design
Turbomachinery

ABSTRACT

In recent years, renewable energy generation has experienced unprecedented growth driven by concerns about climate change. Energy storage systems are essential as bridges between renewable generation and integration in sectors such as industry, where efficient systems integration could promote the decarbonisation of processes. Thermochemical storage systems based on turbomachinery are promising, but they still present challenges when operating under off-design conditions. These systems must be studied under these conditions, since their integration into sectors such as industry, where generation and demand fluctuate, can deviate significantly from their rated conditions. In this sense, an exergy study based on off-design models and real data on renewable generation and demand could identify bottlenecks in current configurations. This work presents a comprehensive exergy study of the integration of a novel thermochemical system into a real industrial environment, accounting for variable generation and demand, thereby providing a more realistic scenario. The dynamic study, conducted over an annual cycle, reveals thermodynamic limitations and technological integration challenges in turbomachinery that cannot be detected by simpler analyses. In addition, adaptive compression and expansion systems are proposed to mitigate the fluctuating impact, thereby overcoming these challenges and achieving a remarkable exergy performance of 77.8%. The exergoeconomic evaluation yields competitive values compared to current approaches, including a storage cost of $30 per MWh, an exergy-destruction-based cost rate of $6.35/MWh, and an LCOE for photovoltaic generation of $76.21/MWh.

1. Introduction

The global contribution of renewable energy to electricity generation is increasing, reaching up to 20% of total electricity generated [1]. In this respect, generation systems such as wind or solar contribute more than 25% [2]. Photovoltaic energy has the potential to become a significant source of electricity worldwide. This renewable energy is abundant, affordable, and easily scalable, with the unique ability to serve most market segments, from small household systems to utility-scale plants [3]. In addition, it is the fastest-growing source of renewable electricity production and a pillar for the EU's transition [4]. The photovoltaic energy integration into the European industrial sector is experiencing rapid expansion, driven by the need for energy security, decarbonization targets (REPowerEU), and volatile energy prices, and is increasingly adopting photovoltaic systems to ensure energy stability and reduce operating costs [5]. Only a limited number of technologies are considered to mitigate the fluctuating nature of renewable

* Corresponding author.
E-mail address: jguisado1@us.es (J.M. Guisado).

https://doi.org/10.1016/j.apenergy.2026.128241
Received 17 April 2026; Received in revised form 25 May 2026; Accepted 9 June 2026
Available online 16 June 2026
0306-2619/© 2026 The Authors. Published by Elsevier Ltd. This is an open access article under the CC BY-NC-ND license (http://creativecommons.org/licenses/by-nc-nd/4.0/).

Nomenclature

Abbreviations

P_r	[−] Performance Ratio
P	[bar] Pressure
G	[W/m^2] Irradiance
PV	Photovoltaic
A_{PV}	[m^2] Installed photovoltaic area
η_i	[−] Isentropic efficiency
W	[kW] Power
T	[K] Temperature
h	[kJ/kg] Enthalpy
S	[Kj/°C] Entropy
ρ	[m^3/kg] Density
V	[m^3] Volume
x	[%] fraction mass
PR	[−] Pressure ratio
m	[kg/s] Mass flow rate
ε	[−] Heat exchanger effectiveness
NTU	[−] Heat Transfer Units
Q	[kW] Thermal power
C_p	[kJ/kg°C] heat capacity
n_o	[hour]Operating hour
γ	[−] Heat capacity ratio
CaL	Calcium Looping

Subscript

in	Inflow
out	Outflow
car	Carbonation
cal	Calcination
av	Average
C	Compressor
T	Turbine
HX	Heat exchanger
0	Reference state
d	Rated design
min	Minimum
max	Maximum
s	Isentropic process
P	Product exergy
F	Fuel exergy
D	Exergy destruction

Superscript

$CaCO_3$	Calcium carbonate
CaO	Calcium oxide
CO_2	Carbon dioxide
re	Reactor

generation, with thermal and thermochemical energy storage systems being promising approaches given their performance and could bridge the gap between generation and demand for medium-scale systems such as the industrial sector [6,7]. While these integrations offer an opportunity to improve decarbonization in the industrial sector, they present challenges due to inefficiencies in current systems caused by the fluctuating nature of generation and demand [8,9].

The industrial sector accounts for a significant portion of energy consumption, generating 25% of global carbon emissions. In Europe, in particular, this sector consumes around 3000 TWh of energy per year, of which only about 300 TWh come from renewable sources [10]. More than 65% of this energy is used for heating. In this regard, steam generation plays a vital role in processes such as heating and drying, which implies the decarbonization of steam production as a critical step for the decarbonization of the industrial sector [11]. Despite the widespread assumption that this demand requires a constant thermal baseline, production processes intrinsically generate significant spatiotemporal fluctuations and transient load requirements. These dynamics stem from multiple factors: batch-processing operations, variations in ambient temperature affecting facilities, shifts in capacity planning, and diverse temperature ranges required across subsectors. Furthermore, because up to 89% of high-temperature industrial heat can be economically addressed through clean and renewable energy, understanding this temporal variability is critical. Properly modeling variable load profiles enables more accurate system sizing, the integration of TES, and optimized power-to-heat strategies, all of which are vital to decarbonizing heavy industry while maintaining economic viability [12].

TES systems can be classified by their operating temperature or storage mechanism (e.g., sensible or latent heat). Sensible heat storage is a mature technology, with large commercial plants utilizing molten salts in concentrated solar thermal power (CSP) plants [13]. Recently, state-of-the-art TES has shown potential for integration with photovoltaic or wind systems as an alternative to electrochemical batteries [14]. Thermochemical Energy Storage (TCES) is a highly promising approach that improves overall energy performance, offering greater energy storage density, higher maximum heat discharge temperatures, and long-term storage capacity [15]. TCES systems minimize heat transfer to the environment, reducing heat losses and enabling long-term storage at near-ambient temperatures. Despite these advantages, TCES is still in its early stages of development and is primarily studied in laboratory environments [16]. In recent years, TCES integration has extended to the industrial sector, where small to medium-sized storage systems (1–10 MW) are efficiently utilized for off-grid and self-consumption applications. Various studies highlight the potential and challenges of these integrations [17]. For instance, one work [18] analysed the challenges of calcium looping-based TCES in the industrial sector, emphasizing “off-design” operational behavior as a major hurdle, although it was not addressed. However, in [19] the off-design behavior when integrating similar systems in CSP plants was investigated. When adapting TCES for industrial applications, studying the variable nature of energy demand—rather than just generation—is crucial. Furthermore, a study in [20] on calcium looping-based TCES integrated with CSP identified identical challenges, determining that they currently hinder commercialization and highlighting further industrialization as the necessary pathway forward.

TCES systems operate via reversible chemical reactions, storing thermal energy as chemical bond energy. During the charging step, heat from an external source drives an endothermic dissociation, yielding separate reaction products that can be stored indefinitely at ambient temperatures. When energy is required, these products are recombined, triggering the reverse exothermic reaction and releasing the stored thermal energy [21]. TCES technologies are typically classified by their reaction type and material nature. Solid-gas reactions are especially promising for large-scale utility, as the primary solid products are easily contained [22]. Leading candidates include reversible systems based on metal hydrides [23], metal oxides [24], hydroxides [25], and carbonates [26]. Carbonates are highly favored for their high operating temperatures, low operating pressures, high volumetric energy density, and benign, non-corrosive chemical composition. Among carbonate systems, the calcium looping (CaL) process has emerged as a premier technology. Compared to alternative storage systems (e.g., molten salts), CaL provides superior energy density, well-established industrial-scale components, a flexible operating temperature range, and highly affordable raw materials. CaL process achieve energy densities of up to 3.2 MJ/m^3,

enabling a threefold volume reduction compared to conventional sensible heat systems. Unlike molten salt-based storage, which is limited to 200–650 °C to prevent degradation, CaL systems operate at temperatures up to 900 °C and deliver round-trip conversion efficiencies exceeding 40% [15]. Chacartegui et al. [27] demonstrated the integration of CaL in concentrated solar power (CSP) plants, achieving overall efficiencies up to 45%, while subsequent studies [28] have proposed advanced configurations to further enhance cycle viability. Recently, Ortiz [15] introduced a modular TCES battery utilizing a single reactor for both calcination and carbonation, improving scalability and integration with renewable sources. Although research on coupling CaL with intermittent renewables like wind and photovoltaics (PV) remains limited, recent works have explored using excess PV generation to drive CaL systems in both utility-scale [29] and residential [30] applications. A primary challenge in these systems is the multicyclic deactivation of regenerated CaO, where conversion rates decline significantly over successive calcination/carbonation cycles [31]. To mitigate this degradation, various strategies have been proposed, including the continuous addition of fresh CaCO3 make-up [32], the use of advanced CaO precursors [33], thermal pretreatments [34], and the optimization of reactor operating conditions [35].

Off-design conditions can significantly deviate systems from nominal operating points, leading to increased energy losses that fluctuate hourly when integrated with intermittent resources or variable demand. Although critical, many studies overlook fluctuating generation and time-varying demand in the industrial sector [36]. Analyzing these combined dynamics is essential to estimate thermodynamic losses and identify technological limitations. While previous literature has evaluated storage systems, such as TES [37] and TCES [38], under off-design conditions, exergy analysis remains a highly effective framework for evaluating these operational shifts [8,39]. Specific investigations underscore the value of exergy assessments in this context. The conditions that minimize exergy destruction in TES components have been identified [40], alongside studies analyzing off-design impacts on turbomachinery, such as the behavior of CO_2 as a working fluid in axial turbines for CSP systems [41–43]. Similarly, integrated systems demonstrate the importance of off-design modeling: one study on a CaL-CSP system found that energy efficiency can vary by up to 17.6% based on solar profiles. Furthermore, optimizing key parameters like carbonation temperature and mass flow rate in integrated CaL storage setups can significantly improve exergy efficiency [44]. Other exergy analyses highlight critical system irreversibilities, yielding exergy efficiencies between 28.6% and 31.5% [45], while modeling annual cycles has proven vital for capturing more realistic, long-term results [46]. Despite the depth of these specialized contributions, the fluctuating nature of industrial demand, a crucial parameter for practical implementation, is frequently neglected in the current literature. The current configurations of TES and TCES systems are based on turbomachinery, such as compressors and turbines, which are particularly sensitive to load variations. However, these limitations are overlooked in energetic or exergetic analyses that do not integrate off-design models when operating under variable loads. Studies such as [19,37,38] do not consider this combination of models, which can demonstrate the actual limitations of the systems under off-design conditions. Although some works have shown the limitations or advantages of optimizing compression or expansion processes when the system operates under off-design conditions [9,47], they do not combine exergy models with off-design behavior and variable load and demand. In general, these lead to a drastic drop in isentropic efficiency, aerodynamic instability, increased auxiliary consumption, and thermal stress on the blades.

Exergoeconomic analysis is a superior methodology for evaluating energy systems, linking thermodynamics and economics to reveal inefficiencies and cost allocations hidden by conventional energy analyses. Numerous studies validate its critical role in optimizing and establishing the economic viability of energy storage and renewable systems. For example, when evaluating TES under rated conditions, studies report electricity costs of $0.0783 kWh and a payback period of 3 years [48]. Similarly, when applied to a geothermal power system, researchers calculated a short payback period of 3.20 years [49]. In a related study, Yousef [50] assessed a solar still coupled with TES at rated conditions, yielding an electricity cost of $0.083–$0.128/kWh. An exergoeconomic assessment of a TCES system based on CaL has also been performed [51]. However, a common limitation across these studies is their reliance on steady, rated design conditions; they generally overlook off-design operations that are necessary to reflect the natural fluctuations of renewable energy sources [48,51].

Table 1 presents a comparison of selected energy storage technologies for industrial applications, considering key indicators such as exergy efficiency, operating temperature, energy density, cost, and off-design adaptability.

Although the growing integration of renewable energy addresses sustainability goals, it introduces significant fluctuations that challenge industrial integration. The highly variable nature of industrial demand and renewable generation profoundly impacts TCES systems, which remains a critical gap in current research. Because TCES systems are traditionally based on turbomachinery, they are exceptionally sensitive to fluctuating operating conditions. Furthermore, their off-design performance remains insufficiently explored, particularly regarding the variable demand that is crucial for the unloading stage. To address these challenges, this study presents a comprehensive annual exergetic evaluation based on real-world industrial generation and demand data, specifically modeling the system's off-design behavior. We also propose and evaluate novel strategies to buffer the impact of variable loads on the turbomachinery, analyzing them through detailed exergoeconomic and exergetic studies of key system parameters. The proposed solutions effectively mitigate these challenges, demonstrating improved operational integration and stability. The system achieves a high exergy performance of 77.8%, with the exergoeconomic assessment yielding highly competitive metrics: an LCOS of $30/MW, an exergy destruction cost rate of $6.35/MWh, and an LCOE of $76.21/MWh.

2. Process diagram flow and operation mode

Fig. 1 shows the process flow diagram of the system under study, based on TCES with CaL and with an adaptive compression/expansion strategy. The basic concept and initial operating conditions for the storage system were proposed in [15]. The electrical energy used by the reactor heaters is supplied by a PV system, indicating that the system's input is a renewable resource, and the reactor is considered a fluidised bed reactor. The heat generated by heaters can be stored as sensible energy or as chemical energy, depending on the reaction temperature. First, the electrical energy is stored as sensible heat until the temperature of the stored solids reaches the calcination temperature, which is 900–930° at 1 bar. When the calcination conditions are reached, the reactor uses electrical energy to drive the endothermic reaction, transforming the stored solids (reactants) into reaction products. The reversible reaction equation representing the $CaCO_3$/CaO energy storage system is shown in Eq. (1).

$$CaCO_3\ (solid) \leftrightarrows CaO\ (solid) + CO_2\ (gas)\ \Delta H_{re} = \pm 178 kJ/mol \quad (1)$$

The products, the CaO remains in the reactor, while the carbon dioxide joins the CO_2 heat transfer stream that evolves through for cooling, compression, and storage. The CaO could be used to store sensible heat after calcination. Still, its system capacity to store sensible heat is limited to avoid problems such as sintering, with a maximum temperature of 1100 °C. The reactor operates at around 1.1 bar, and the maximum pressure drop threshold of the gas entering the reactor is set to 15%. During charging, the excess CO_2, acting as a heat-transfer working fluid, enters the reactor, promoting a bubbling regime at a velocity of 0.25 m/s. During discharge, the compressed and stored CO_2 passes through a turbine system to recover energy while decreasing its pressure before entering the reactor, where CaO and unreacted $CaCO_3$ remain,

Table 1
Comparison of selected energy storage technologies for industrial applications.

Technology	Exergy efficiency [%]	Temp range [°C]	Energy density [kWh/m^3]	Off-design adaptability	Industrial integration	Reference
Molten salt TES	30–50	250–650 °C	70–200	Medium	High	[13]
CAES	40–70	<600 °C	3–24	Medium	Medium	[52]
Li-ion batteries	85–95	<100 °C	150–400	High	Limited	[53]
sCO_2 storage systems	30–70	300–700 °C	20–25	Medium	Emerging	[54]
This work (CaL)	~77.8	up to 900 °C	350–700	High (adaptive)	High (modular)	

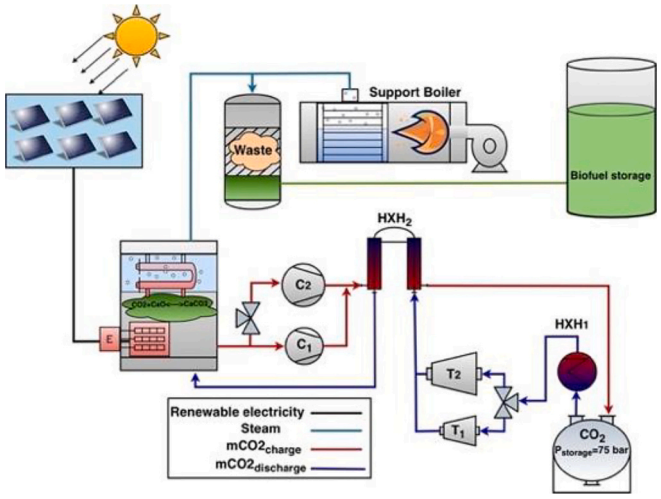


Fig. 1. System schematic.

acting as a carbonator. The exothermic carbonation reaction releases thermal energy that, in this case, is transferred to saturated water, producing steam to power a digester for biofuel generation. The working conditions will depend on the process, which in this work is saturated steam at 8 bar.

In this case study, the PV system produces electrical energy only for the storage system, which is charged and discharged daily. The storage system must ensure that the calcination reaction occurs, so that when the system reaches these conditions, the PV energy is used entirely to transform reactants into products. The system also integrates heat exchangers to increase efficiency and ensure the reactor's operating conditions. The distinctive feature of the modular layout is based on the work by Ortiz et al. [15]. The modules are designed to fit a standardised 24-ft shipping container. In this aspect, and to optimise transport, 10 storage cylinders whose diameter is 1.1 m and length is 2.43 m, which optimise transport, this configuration allows a free volume for the rest of the components of 11.84 cubic meters and a storage energy volume of 23.1 cubic meters.

Variable performance analysis of turbomachinery shows that integrating compressors and turbines that adapt to operating conditions significantly reduces exergy destruction and can improve cost indices in an exergoeconomic study. However, it could also improve energy performance, as reported in [9] During charging, before the reactor reaches carbonation conditions, a minimum CO_2 mass flow rate is required to promote a bubbling regime, ensure efficient gas-solid contact, and facilitate heat and mass transfer during carbonation. The smaller compressor, C_1, manages this mass flow rate. During the reaction, the mass flow rate increases, and the larger compressor, C_2, controls it. The turbines operate similarly. During charging, the smaller turbine, T_1, controls the mass flow rate. During the discharging step, when the flow rate is higher and variable, it is controlled by the larger turbine, T_2.

3. Modeling approach

This work has developed a mathematical model to evaluate the system's energy and exergy behavior, including mass, energy, and exergy balances. A quasi-stationary simulation is run hourly to assess performance over the whole year. The thermodynamic model of the system has been developed in EES (Engineering Equation Solver).

3.1. Photovoltaic system

This study considers an 8 MW photovoltaic system. Its performance is evaluated using the Performance Ratio (P_r) model, consistent with previous studies [53], as defined in Eq. (2). This model calculates the photovoltaic output as a function of environmental conditions and input power. The average hourly P_r values throughout an annual cycle, which range between 0.68 and 0.87, are presented in Appendix A (Fig. A1). In this context, W_{pho} represents the PV power and A_{PV} denotes the PV area, totaling 48,200 m_2. The P_r values depend on environmental data provided by the GTER (Thermodynamics and Renewable Energy Group) of the University of Seville (Appendix A) for the year 2019, corresponding to a facility located in Seville, Spain. This information and models have been used in other works in the literature [8,9]. Furthermore, this system integrates an electric heater (EH) as an alternative to renewable heat generation. While photovoltaic energy has lower efficiency than solar thermal systems, resulting in lower cost-effectiveness and land-use efficiency, it offers unique advantages, such as higher fluid temperatures, which enable charging high-temperature, low-cost thermal energy storage systems. [55]. In [56], the integration of PV + EH and molten salt storage for large-scale applications is reported to have yielded satisfactory results. Furthermore, they note that the recent, drastic decrease in photovoltaic costs more than compensates for the considerable loss of efficiency. A techno-economic evaluation of a hybrid solar thermal and photovoltaic energy storage system with an electric heater for the sustainable production of industrial steam was studied in [55], achieving good economic results and providing up to 60% of the demand.

$$W_{pho}\,[W] = P_r \bullet A_{PV} \bullet G_{poa} \tag{2}$$

3.2. Energy storage system

In this work, the maximum conversion of multicyclic carbonation reaches 0.15, which would enable a process without the addition of fresh material and under harsh carbonation and calcination conditions, in line with similar works [15]. In [57] a sensitivity study based on maximum conversion showed that a variation between 0.1 and 0.4 resulted in a moderate variation in efficiency and a considerable increase in the storage vessel volume to achieve the same energy storage capacity. According to the kinetic model proposed in [35], Appendix B, this work assumes that the reaction rate is sufficient to produce the maximum achievable carbonation (x = 0.15) in a period of one hour, if the reactor temperature is between 400 and 875 °C (carbonation), and that no carbonation occurs if it is outside this range. This approximation has been considered in other similar studies [15], since, although

carbonation also occurs in an atmosphere of pure CO_2 at atmospheric pressures below 400 °C, the reaction rate decreases considerably [58,59]. Therefore, carbonation at lower temperatures can be disregarded for this approximation over a period of one hour. Using a similar approach, the carbonation rate near the equilibrium temperature can also be disregarded [60]. The CO_2 storage pressure is assumed to be kept at a constant 75 bar. This simplification is conservative, as the storage is partially empty for much of the year, reducing the compressor's energy consumption when compressing CO_2 to the actual storage pressure rather than the maximum limit. This work assumes that CO_2 leaves the reactor at a temperature 200 °C lower than that of the solids. Thermal losses in the reactor are considered to be 0.1% per hour of the stored heat. [61]. In heat exchangers, a minimum temperature difference of 20 °C and an overall heat transfer coefficient of 50 W/(m^2k) are assumed [15]. The cooling stage before compression assumes an outlet temperature of 25 °C to reduce compression work.

3.2.1. Mass balances

The average mass of products in the reactor in the initial situation is defined in Eqs. (3)–(7). The subscript i represents CaO or $CaCO_3$ at the beginning of the reaction, which is associated with the type of reaction and the considerations of this work. The volume of the reactor, $V^{reactor}[m^3]$ is 2.34 m^3 and n^{re} is the number of reactors, which is optimized in section 4.1. m_i^0 depends on the initial situation, which depends on the fraction of solids, $x_i^0[-]$.

$$m_{av}^{re}[kg] = V^{re} \bullet \rho_{av}^{re} \tag{3}$$

$$m_{av}[kg] = n^{re} \bullet m_{av}^{re} \tag{4}$$

$$m_i^0[kg] = x_i^0 \bullet m_{av} \tag{5}$$

$$\rho_{av}^{re}\left[kg/m^3\right] = \rho_{av} \bullet PD \tag{6}$$

$$\rho_{av}\left[kg/m^3\right] = \rho_{CaO} \bullet x_{CaO} \bullet \theta_{CaO} + \rho_{CaCO3} \bullet x_{CaCO3} \bullet \theta_{CaCo_3} \tag{7}$$

where ρ_i represents the density of each material, $\theta_{CaO} = 0.5$ is the CaO porosity, and PD = 0.6 is the packing density [62].

In this work, it is assumed that carbonation occurs at reactor temperatures below 400 °C under atmospheric pressure. From that temperature onward, the reaction kinetics are very slow as we approach equilibrium, so it is assumed that, from 875 °C onward, there is no carbonation [63].

In this work, the exergetic study is performed hourly, implying that the mass and energy balances are computed hourly over the year. Eqs. (8)–(11) define the balances for each hour and type of system component.

$$m_{car}^{CaO} = x_{car}(i) \cdot m^{CaO}(i-1) \tag{8}$$

$$m_{car}^{CaCO3} = m_{car}^{CaO}(i) \cdot \frac{M_{CaCO_3}}{M_{CaO}} \tag{9}$$

$$m_{car}^{CO_2} = m_{car}^{CaO}(i) \cdot \frac{M_{CO_2}}{M_{CaO}} \tag{10}$$

$$Q_{car} = \Delta H_{re}(i) \bullet m_{car}^{CaCO3} \tag{11}$$

where x_{car} [−] is the conversion degree in the carbonation reaction, ΔH_{re}[kj/kg]] is the enthalpy of reaction under the reaction conditions, which is assumed to be constant for the conditions under study with a value, in line with similar studies [15,57], of 178 kJ/mol. Q_{car}[kW] is the thermal power of carbonation, which is an exothermic reaction, and M_{CaCO_3}, M_{CO_2} and M_{CaO} [g/mol] are the mass molar. The mass of CaCO3 or CaO in the reactor varies hourly according to Eq. (12). The sign (±) represents the increase or decrease of materials amount depending on the stoichiometric coefficients.

$$m_j(i) = m_j\,(i-1) \pm m_{j,reac}(i) \tag{12}$$

When the conditions in the reactor are not the conditions for the carbonation reaction to occur, the mass flow rate of CO2 is the minimum that ensures bubbling, $m_{min}^{CO_2}$ if the conditions in the reactor allow carbonation, the mass flow rate is the CO2 produced in the reaction.

When calcination conditions occur ($930 > T_{re} > T_{max}$ and $m_{CaCO3} > 0$) Eqs. (13)–(14) define the reaction.

$$Q_{cal} = \Delta H_{re}(i) \bullet m_{cal}^{CaCO3} \tag{13}$$

$$x(i) = x(i-1)(1 - x_{cal}(i)\,) \tag{14}$$

where x_{cal}, calcination degree is one if the complete $CaCO_3$ decomposition occurs. In this case, x becomes zero, and the carbonation can later occur again, up to x_k (as maximum).

3.2.2. Energy balances

The thermal balance, Q_b[kW] can be defined by eq. 15, which is composed of the photovoltaic power (Q_{PV}) that enters the system and the different consumptions in the form of thermal powers, which are: the power demanded in the process (Q_d), the power associated with the mass flow of CO2 (Q_{CO_2}) and the power lost associated with the losses to the environment (Q_l).

$Q_b(i)[kW] = Q_{PV}(i) - Q_d(i) - Q_{CO_2}(i) - Q_l$ (i) (15).

Sensible thermal power of the solids stored in the reactor, Q_s[kW] can be related to the power balance and the heat of the reaction (Q_r) which can be exothermic (+) in carbonation and endothermic (−) in calcination, Eqs. (16)–(17).

$$Q_s(i)[kW] = Q_b(i) \pm Q_r(i) \tag{16}$$

$$Q_s(i)[kW] = \sum_{j=CaO,CaCO_3} m_j(i) Cp_j(i) \left(T_{re}(i) - T_{re}(i-1) \right. \tag{17}$$

Eqs. (18)–(19) allow the thermal power in the CO_2 mass flow and the thermal power lost to the environment to be obtained, which is considered to be 0.5% of the heat stored in the solids, CaO and CaCO3 [15].

$$Q_{CO_2}(i)[kW] = m_{in}^{CO_2}(i) Cp_{CO_2}(i) T_{in}(i) - m_{out}^{CO_2}(i) Cp_{CO_2}(i) T_{out}(i) \tag{18}$$

$$Q_l(i)[kW] = 0.005 Q_s(i) \tag{19}$$

The energy balances, based on the mass balances, are developed hour by hour for different i hours throughout the year.

3.2.3. Power cycle

In turbomachinery and exchangers, the first law of thermodynamics is applied, as defined by Eq. 20 for turbines, Eq. 21 for compressors, and Eq. 22 for heat exchangers, which have been used in similar works [64].

$$W_T[kW] = m_{CO_2}(h_{in} - h_{out}) \bullet \eta_{iT} \tag{20}$$

$$W_C[kW] = m_{CO_2}(h_{out} - h_{in})/\eta_{iC} \tag{21}$$

$$Q_{HX}[kW] = m_{CO_2}(h_{out} - h_{in}) \tag{22}$$

where ηi_T and ηi_C are the isentropic efficiencies of the turbine and compressor, respectively, in this work, the efficiencies of the turbomachine and heat exchangers are not constant. In this respect, the isentropic efficiencies can be affected by the photovoltaic energy input and the discharge rate. The models for evaluating compressor and turbine efficiency under off-design conditions, along with their numerical validation, are presented in Appendix C.

The area of the heat exchangers can be obtained using the Number of Transfer Units (NTU) in Eq. (23), as used by other authors [65]. Where F is the correction factor, A is the area, U is the overall transfer coefficient,

and ΔT_{lm} is the log mean temperature difference. In the case of gas-gas exchangers, according to other similar work [15], it is possible to assume $F = 0.92$ and $U = 80 W/(m^2 k)$.

$$Q_{HX}[kW] = U \bullet A \bullet F \bullet \Delta T_{lm} \quad (23)$$

3.3. Exergy balances

The specific exergy, e[kJ/kg] of each material stream can be expressed as the sum of the different exergies involved, which can be calculated according to Eq. (24), kinetic e_k, chemical e_{ch}, physical e_{ph} and potential e_p. It is normal to assume that kinetic and potential exergy can be neglected as neither the total plant height nor the incoming and outgoing streams velocities are being considered. This implies that the sum of the physical and chemical exergy constitutes the total exergy of a stream. The specific exergy e accounts for the deviation between actual and standard environmental conditions [66]. The exergy of the stream can be calculated from Eq. (25), where $N_i[mol/s]$ is the molar flow of component i.

$$e_i[kJ/mol] = e_{ph} + e_{ch} + e_k + e_p \quad (24)$$

$$E_i[kW] = N_i e_i \quad (25)$$

The physical molar exergy of stream i can be calculated from Eq. (26) [45].

$$e_{ph}[kJ/mol] = (h_i - h_0) - T_0(S_i - S_0) \quad (26)$$

Each material stream exergy is evaluated according to the reference state, which have been consistent with the standard environmental conditions ($T_0 = 298$ K and $P_0 = 101325$ Pa). Where h_i and S_i are the enthalpy and entropy, respectively, of the stream under the conditions of the stream i [66].

The chemical molar exergy of stream i can be calculated as:

$$e_{ch}[kj/mol] = \Delta G_f + \sum_e n_e \varepsilon_{che} \quad (27)$$

where ΔG_f is the Gibbs free energy of the chemical function of compound *j*, n_e is the stoichiometric coefficient of the constituent element *e* of the compound i, and ε_{ch} is the chemical exergy of the constituent element *e*, which is the standard molar chemical exergy of the compound [67]. The values have been obtained from similar works: 5.05, 119.62, 20.14, 3.12, and 11.71 MJ/kmol for CaCO3, CaO, CO_2, water and steam, respectively [45,67].

The exergy equation for the k-th component is as follows.

$$E_{F,K} = E_{P,K} + E_{D,K} \quad (28)$$

where $E_{F,K}$, $E_{P,K}$ and $E_{D,K}$ are the fuel, product, and exergy destruction of the k-th component, respectively.

The processes of the different elements can be analysed from an exergetic point of view using exergy efficiency (ε_k) and exergy loss rate (y_k) which can be defined as:

$$\varepsilon_k = E_{P,K}/E_{F,K} \quad (29)$$

$$y_k = E_{D,K}/E_{F,K} \quad (30)$$

Many researchers have studied the exergy of the solar radiation. The different equations they propose show similar results. This work uses Eq. (31), proposed by Petela in 1964 [68], which has been used in similar works [45,68].

$$E_{D,Solar}[kW] = G_{POA} \bullet A_{PV} \bullet G_{poa} \bullet \left[1 - \frac{4}{3} \bullet \frac{T_0}{T_{sun}} + \frac{1}{3} \bullet \left(\frac{T_0}{T_{sun}}\right)^4\right] \quad (31)$$

where T_{sun} is the surface of the sun temperature, which in this work is 5600 K according to other works [45].

3.4. Adaptative turbomachinery strategies

Sections 4.2.2 and 4.3.1 demonstrate unstable behavior for the compressor and turbine, respectively, based on variations in the CO_2 flow rates circulating through the TCES. This reveals unacceptable technological or thermodynamic limitations for the system, primarily due to extreme fluctuations in mass flow rate. System analysis highlights these variations during both the loading and unloading stages. During the loading stage, the system operates with the minimum flow rate necessary to promote bubbling until calcination reaction conditions are reached. From this point, the calcination reaction produces CO_2, sharply increasing the flow rate, a spike further amplified by incoming solar power.

To address this, the expansion process presents a similar scenario switching strategy is proposed using the following logic: when the circulating flow rate reaches the minimum required for bubbling (0.25 kg/s), a three-way valve diverts the flow to a compressor optimized for this baseline mass flow rate. Once the reaction begins and the flow rate exceeds 0.25 kg/s, the three-way valve switches to divert the flow to compressor C_2, which is sized to handle the higher CO_2 flow rates produced during calcination. The expansion process presents a similar scenario, during the loading stage, the system expands the minimum flow rate to promote bubbling and utilize energy. Conversely, during the unloading stage, it must manage the CO_2 flow rate from the carbonation reaction, which fluctuates depending on the discharge rate. This makes it difficult for a single commercially available turbine to handle the entire range of flow rates while maintaining acceptable thermodynamic performance. Therefore, the proposed strategy expands the minimum flow rate through a dedicated turbine, utilizing a larger turbine for the higher flow rates generated during the carbonation reaction. A valve before the turbine inlet directs the flow to the appropriate turbine depending on the system stage.

3.5. Model simplification, boundary conditions and validation

This section summarizes the model considerations and the boundary conditions taken into account to simplify the resolution of the problem under study.

1) The reaction kinetics follow the model shown in Appendix B, with a maximum conversion of multicyclic carbonation of 0.15, although the impact of varying this parameter is subsequently explored. The model neglects solid composition and carbonation during the diffusion stage under the proposed reactor conditions [35]. Furthermore, it is established that this conversion is achieved within one hour, which is fundamental to the considered time basis.
2) The reference state for exergy coincides with a temperature (T_0) of 298 K and a pressure (P_0) of 1 bar.
3) Hourly heat losses to the environment are assumed to be 0.5% of the stored heat, based on similar studies.
4) The equipment efficiency conditions for the heat exchangers, F and U, are considered constant, with values of $F = 0.92$ and $U = 80$ W/m_2/K, based on other similar works [15].
5) This study assumes that under initial conditions (00:00, January 1st), the storage system starts at half capacity. This represents 27 MWh of stored energy, with the CO_2 at 75 bar and a reactor temperature of 900 °C. This is a conservative assumption for a one-year period, as the system typically stabilizes within a few days.
6) The convergence tolerance for hourly mass and energy balances was set to 10^{-3}. This threshold guarantees that the iterative relative error satisfies fundamental conservation laws while avoiding excessive computational slowdown.
7) The enthalpy of reaction under the reaction conditions is assumed to be constant for the conditions under study, with a value, in line with similar studies, of 178 kJ/mol [15].

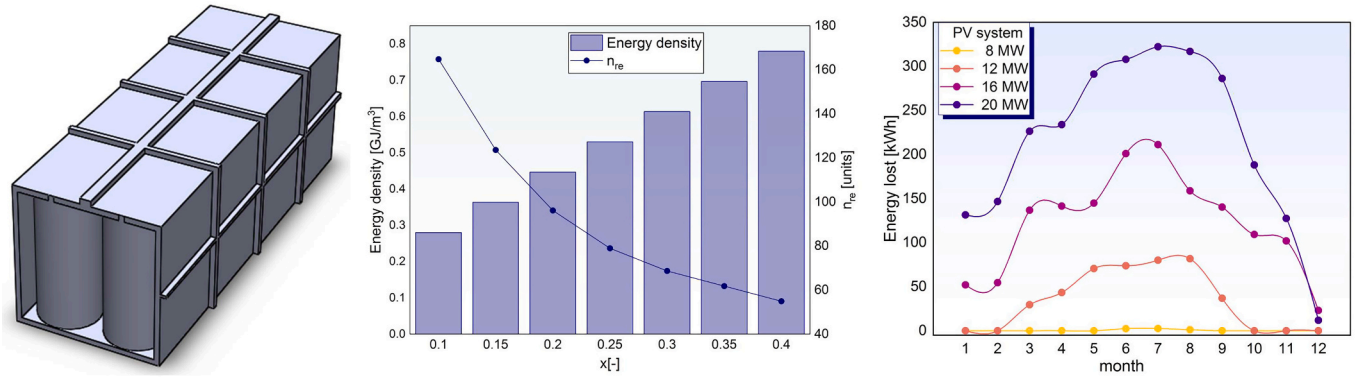


Fig. 2. a) Container ship with storage capacity of 23 cubic meters with 10 cylindrical modules of 2.3 cubic meters; b) Average unusable energy per day from the storage system for different months of the year, depending on different photovoltaic systems.

8) The range of off-design models is based on isentropic efficiency values, ranging between 54% and 87% for the compressor, and between 51% and 90% for the turbine. This serves to avoid the surge region in the case of the compressor and sudden drops in entropy for the turbine, with the maximum values being based on the rated conditions [57].

The developed thermodynamic and off-design model has been validated against reference models and data reported in the literature for similar TCES and turbomachinery systems. First, key thermodynamic outputs such as reactor temperatures, pressure levels, and system efficiencies were compared with previously published studies on CaL-based TCES systems under comparable operating conditions [15,57]. The results show good agreement, with deviations generally within the range of 3–7%, which is considered acceptable for system-level simulations of this complexity. Second, the off-design turbomachinery model was validated by comparing predicted trends in isentropic efficiency and pressure ratio with established correlations and experimental datasets reported for CO_2-based compressors and turbines [47,69]. The model successfully reproduces the expected degradation in efficiency under off-design conditions, consistent with prior studies. Additionally, the model ensures conservation of mass and energy with a convergence tolerance of 10^{-3} in all hourly simulations, guaranteeing numerical stability over the annual cycle.

It should be noted that experimental validation of fully integrated TCES systems under industrial conditions is currently limited in the literature. Therefore, the present validation relies on benchmark comparisons with validated sub-models and previously published works, a methodology widely adopted in system-level studies of emerging energy technologies [45].

Overall, the validation results support the reliability of the proposed model for evaluating the thermodynamic and economic performance of TCES systems under realistic off-design operating conditions. This validation framework ensures robust applicability of the model for industrial-scale TCES assessment.

4. Results and discussions

As a case study, this work examines the integration of a CaL storage system with an existing PV system in an organic waste energy recovery plant in Seville, which uses a digester that utilises the steam produced to supply heat to the transformation process. First, this work develops an energy-based optimisation to determine the optimal storage system for the PV system under study, which has a capacity of 8 MW and is used entirely in the TCES. In the following sections, the exergy behavior during charging and discharging is studied to support an exergoeconomic analysis.

4.1. Optimisation energy storage system

The storage system size was optimized to minimize unutilizable photovoltaic (PV) energy, assuming that the PV system is exclusively integrated with the storage system and that all generated energy undergoes daily charge and discharge cycles. Under these considerations, the maximum stored heat, including sensible heat and the heat of reaction, reaches 54 MWh on July 17th. In this regard, a 293 m^3 storage system is required, which can be formed by 127 N_{re}. Using the modularity concept defined in this study, this implies 13 modules or container ships, since each module contains 10 N_{re}. Although this heavily depends on the maximum carbonation conversion, as shown in Fig. 2b, it can decrease considerably for higher maximum conversions. Consequently, Fig. 2b demonstrates that the system's capacity and volume are highly dependent on the maximum carbonation conversion x_{max}. Specifically, due to a strong dependence on energy density, which can vary between 0.1 and 0.8 GJ/m^3 for x_{max} values between 0.1 and 0.4.

The optimized storage system ensures that no photovoltaic energy is wasted and that all generated energy is stored at temperatures below the system's maximum threshold. Fig. 2b illustrates the daily average of unusable photovoltaic energy across different months, highlighting its behavior when the storage system is integrated with varying sizes of photovoltaic arrays. Selecting the appropriate storage capacity is crucial; the data indicates that an 8 MW setup is optimal. Furthermore, integration with a 12 MW system allows for the complete storage of photovoltaic energy during winter months while preserving excess energy in the summer. This situation is even more critical for larger systems, where unusable energy is generated every month. Based on these hypotheses, it is deduced that for isolated systems with daily charge and discharge cycles, the optimal system configuration is approximately 17.25m^3/MW_{PV}. Applying modularity concepts, this implies that a standard container could efficiently integrate with 1.33 MW_{PV} under the studied conditions.

4.2. Charging stage (calcination)

The overall efficiency of the system during the charging stage is affected by the irreversibility of components, including the compressor, turbine, reactor, and photovoltaic system. Therefore, this section examines the impact of key system parameters on these components. Fig. 3a shows the exergy destruction profile of the system under study during the charging stage on the 15th day of each month.

Fig. 3a shows three stages related to the exergetic behavior of the components. The first stage extends from the start of the charging stage until the reaction conditions are reached. The second stage corresponds to the period during which the reaction occurs, and the third stage is the period after its completion. The existence and duration of the stages

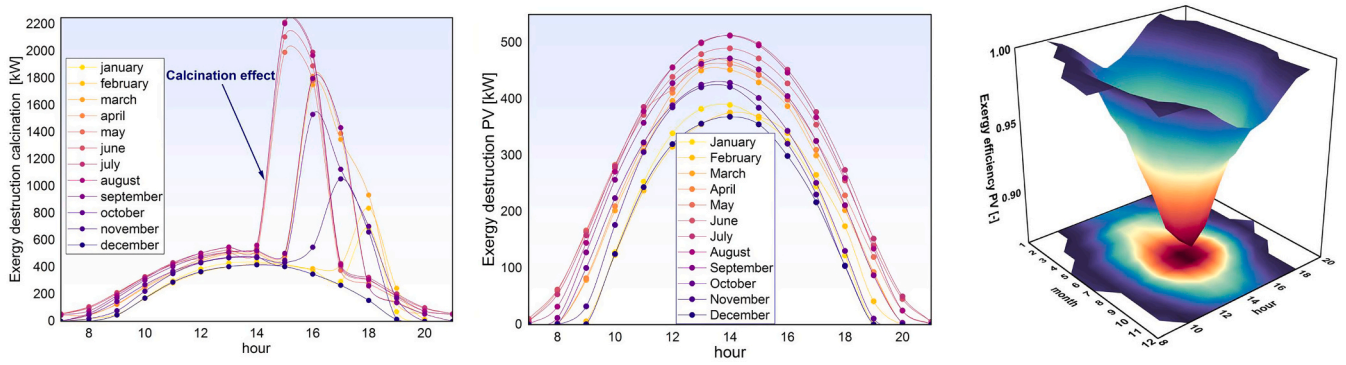


Fig. 3. a) Energy destruction profile of the charging stage on the 15th of each month; b) energy destruction of the photovoltaic system on the 15th of each month; c) energy efficiency of the photovoltaic system over an annual cycle.

depend on the time of year. The duration of the first stage depends on the energy supplied by the photovoltaic system, making it shorter in the summer and starting later in the winter. There are months like January, where the stage lasts 11 h, and even months like December, where the generated energy is insufficient for the reaction to occur. The second stage can last 1 to 2 h in the summer months and 4 to 5 h in the winter months. In the third stage, its duration can vary from 0 h in January or February to 5 h in the summer months. Exergy destruction depends on these stages. In the first stage, it is based on the photovoltaic system, compressor, turbine, and heat exchanger; in the second stage, it must also account for exergy destruction through calcination.

4.2.1. PV system

Exergy destruction in the photovoltaic system depends not on the storage system, but on environmental conditions (Eq. (31)). This behavior significantly affects exergy destruction in the photovoltaic system, thereby affecting the exergy input to the storage system. Fig. 3b shows the exergy destruction of the photovoltaic system as a function of environmental conditions. Exergy destruction is most critical in the summer months and is even more significant at midday, when photovoltaic panel output and solar radiation are higher. Values of up to 528 kW are observed, though they can vary significantly, thereby altering efficiency. Fig. 3c shows the photovoltaic system's exergy efficiency over an annual cycle, which follows the trend of exergy destruction, with values ranging from 0.86 to 0.99. The lowest values are observed during midday and are lower in the summer months, consistent with Fig. 3b and other studies [45].

4.2.2. Compressor

In the compression process, exergy destruction depends on the change in entropy, which in turn depends on the mass flow rate, pressure ratio, inlet temperature, and compressor rated design (Appendix C.1). Fig. 4a and b illustrate the impact of mass flow rate and storage pressure on compressor exergy destruction.

Fig. 4a shows that exergy destruction is more critical at higher storage pressures, as operating at these pressures involves more severe conditions that move the system farther from the reference state (P_0 and T_0). Furthermore, it can be observed that increasing photovoltaic power also increases exergy destruction, since it modifies the exergy efficiency and increases the mass flow rate, which contributes proportionally to this destruction.

Fig. 4b shows a more significant exergy destruction as the mass flow rate increases. This behavior has a linear contribution with increasing mass flow rate and a nonlinear contribution at mass flow rates above the nominal mass flow rate. Furthermore, the impact of operating at lower nominal power levels is observed, as the nominal mass flow rate is also lower, thus increasing the impact of operating at higher mass flow rates. The figure also shows a defined unstable region for mass flow rates between 0.25 and 0.75 kg/s and nominal power levels above 330 kW. This region shows the compressor's unstable operating points due to exceeding the surge margin, as the amount of gas being compressed is insufficient for the compressor's size [70].

Under these conditions, the proposed system can operate at a mass flow rate between 0.25 and 2 kg/s. This means that operating with a compressor whose nominal mass flow rate is between 0.25 and 0.75 kg/s keeps it in the stable operating region, but when operating conditions require higher mass flow rates, energy destruction increases considerably. On the other hand, operating a compressor with a power rating appropriate to the mass flow rate during the reaction reduces exergy destruction at high mass flow rates; however, when reaction conditions are not met, and the mass flow rate is adjusted to promote the bubbling regime, it operates in the unstable region. In this regard, this system operates with two compressors, the C1, whose rated mass flow rate coincides with the minimum mass flow rate to promote the bubbling

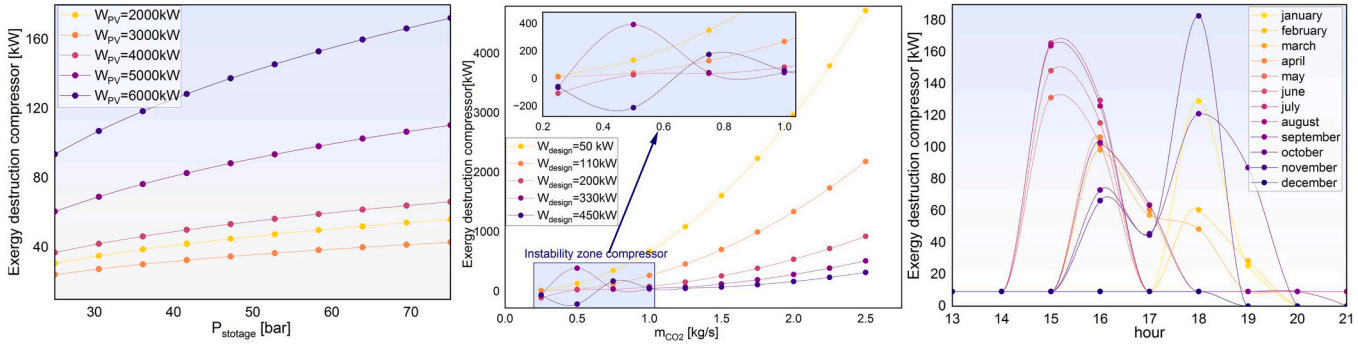


Fig. 4. a) Impact of storage pressure on compressor exergy destruction for different photovoltaic power outputs; b) Impact of mass flow rate on compressor exergy destruction for various rated power; c) Exergy destruction of the compressor with the adaptive compressor strategy on the 15th of each month.

regime and with a pressure ratio in accordance with the system of 75:1 and a nominal power of about 56 kW, operating with an efficiency of 87%. The C2 compressor must manage the mass flow rate generated in the reaction and has been optimized by integrating models over an annual cycle. This optimisation results in a compressor with a rated mass flow rate of approximately 1 kg/s, a pressure ratio of 75:1, and a rated power of approximately 300 kW, operating with an efficiency of 71–87% under off-design conditions. This design ensures that the compressor does not exceed the surge margin for the system's operating conditions.

Fig. 4c shows the compressor's exergy destruction as a function of the photovoltaic profile, using the 15th of each month. It can be observed that in January, February, October, and November, exergy destruction occurs in two stages: the first, based on the minimum mass flow rate, is managed by C1 and remains constant until reaction conditions are reached. The second stage shows a significant increase in exergy destruction due to the reaction, which increases the mass flow rate managed by C_2. The efficiency of C_2 depends on this increase, which in turn depends on the photovoltaic output power. In March, April, May, June, July, August, and September, an additional stage is added, as the supplied energy is sufficient to complete the reaction. This stage, managed by C_1, exhibits exergy destruction similar to that of the first stage, and it ends when the photovoltaic energy is depleted or the solids reach 1100 °C. Furthermore, it shows that December is different, as the system does not reach the reaction conditions, resulting only in the first stage.

4.2.3. Calcination

The calcination stage differs from compression in that it occurs only when the reaction conditions are met. Furthermore, it impacts the various components due to a significant increase in mass flow rate. The key parameters of the calcination process are the reaction temperature and pressure (P_{equi}), which are related (Eq. (32)), and the energy supplied to the reactor, which determines the amount of carbon dioxide produced [58]. Fig. 5a shows the impact of input power on exergy destruction for different reaction conditions. Fig. 5b shows the impact of reference temperature (T_0) on exergy destruction at different input power levels, as calculated using Eq. (26).

$$P_{equi}(atm) \approx 4.083x10^{7} e^{\frac{-20.474}{T_{re}}} \quad (32)$$

Fig. 5a shows that exergy destruction increases with photovoltaic power through a linear relationship with the CO_2 mass flow rate. The figure also shows that operating under more critical reactor conditions increases the physical destruction of exergy, moving the system further from the reference state and increasing the process's irreversibility. These results are consistent with [59]. Fig. 5b shows behavior similar to that in Fig. 5a, but the impact of the environmental conditions considered is less significant. Unlike the operating conditions, it does not move the system further from the reference state, but it does modify it (Eq. (26)).

Fig. 5c shows the exergy destruction in the calcination, which temporally coincides with the reaction. During the peak production months of the year, the summer months, the calcination reaction occurs between 2:00 PM and 4:00 PM, a period of high photovoltaic production. This means that, during these months, exergy destruction reaches high levels, between 1100 and 1400 kW, but in relatively short periods. In months like March or April, the reaction conditions are reached during periods when photovoltaic power is lower, leading to lower values between 200 and 900 kW, but these periods are longer. This is more critical in months like January or February, since the reaction occurs during the last hours of the day, meaning that exergy destruction is very low, even zero in December, because the reaction conditions are not met.

4.2.4. Heat exchanger

The system consists of two heat exchangers, but HX_2 (Fig. 1) has a greater impact during the charging stage than HX_1, as its exergy destruction varies continuously with demand. HX_2 manages the CO_2 produced during calcination or the minimum mass flow rate required to promote the bubbling regime. It also heats the mass flow rate entering the reactor from storage. Eqs. (22)–(23) and (26) for HX_2 show that its key parameters are the reactor temperature, storage temperature, and storage pressure.

Fig. 6a shows the impact of reactor temperature, which increases exergy destruction due to operating under more severe conditions that make the process more irreversible. This impact becomes even more critical as storage pressure increases, for the same reason. This effect is dominant until the reaction occurs; once it occurs, the CO_2 mass flow rate increases, leading to a substantial linear increase in exergy destruction. Fig. 6b shows that, if the reaction conditions are met, exergy destruction increases with photovoltaic energy as higher mass flow rates are generated. Furthermore, the impact is more pronounced at higher storage pressures due to greater irreversibility. Fig. 6c shows the impact of storage temperature, revealing that higher temperatures lead to greater exergy destruction. This impact is even more significant at higher storage pressures, as both factors move the system away from the reference state. The pressure impact is more significant at low temperatures, while at high temperatures, the storage temperature impact is the dominant factor. These results are consistent with the literature. Fig. 7a shows the exergy destruction of the heat exchanger on the 15th of each month.

Fig. 7a shows two or three stages, depending on the month. The first stage begins when the system starts charging, with temperature increase as the dominant factor, resulting in exergy destruction values of 54 to 58 kW. The second stage begins when the system reaches reaction conditions, and the mass flow rate increases considerably, resulting in exergy

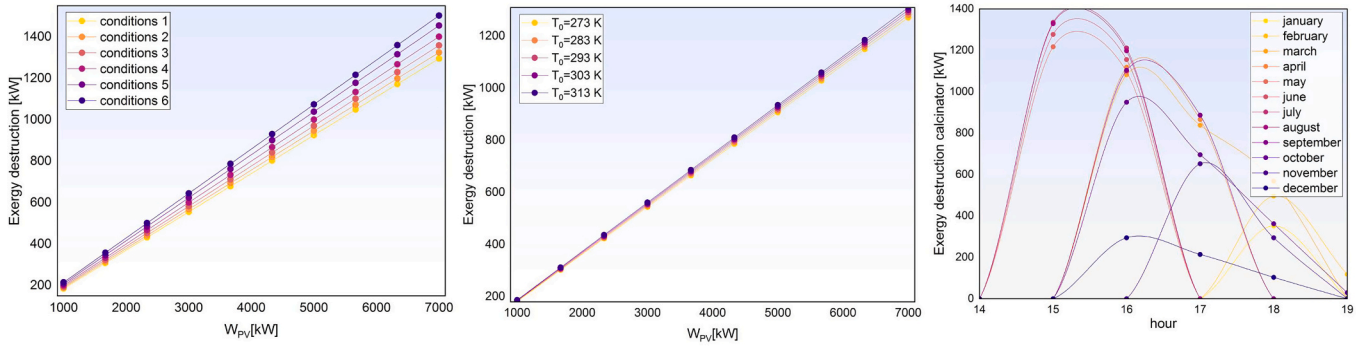


Fig. 5. a) Impact of PV power for different reaction conditions ($P_{reactor}$ d $T_{reactor}$): (conditions 1: $T = 1135$ K and $P = 0.6$ bar; conditions 2: $T = 1144$ K and $P = 0.7$ bar; conditions 3: $T = 1153$ K and $P = 0.8$ bar; conditions 4: $T = 1161$ K and $P = 0.9$ bar; conditions 5: $T = 1168$ K and $P = 1$ bar; conditions 6: $T = 1174$ K and $P = 1.1$ bar); b) Impact of photovoltaic power for different environmental conditions (T_0); c) Exergy destruction of the calcination on the 15th of each month.

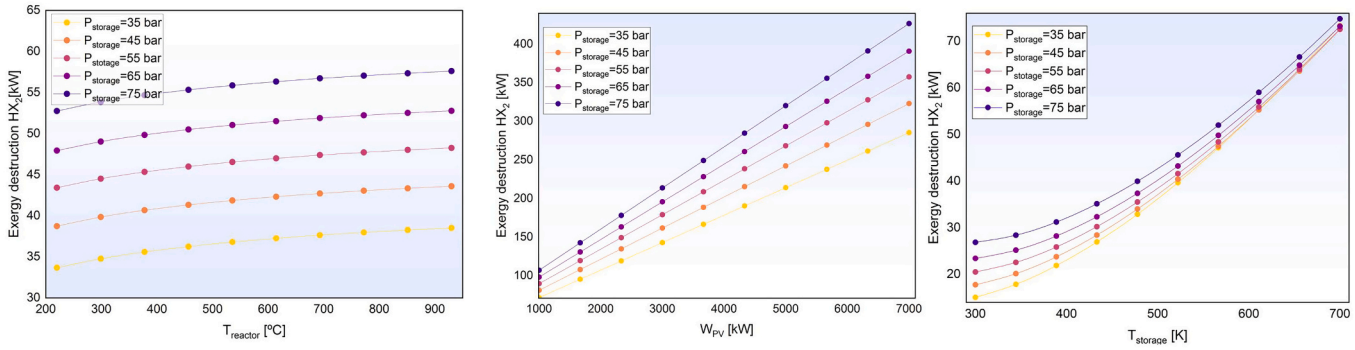


Fig. 6. Impact of key process parameters on exergy destruction of HX_2. a) Reactor temperature for various storage pressures; b) Photovoltaic power output for various storage pressures; c) Storage temperature for various storage pressures.

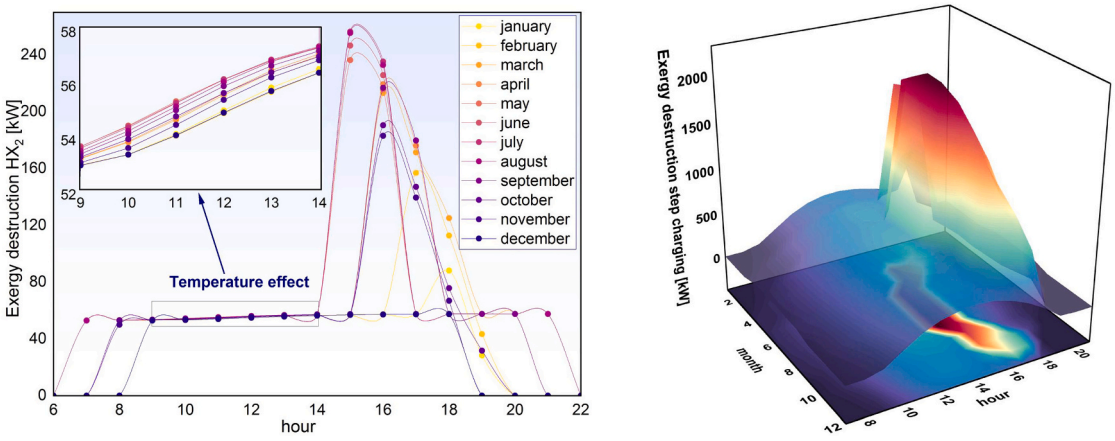


Fig. 7. Exergy destruction of heat exchanger HX_2 on the 15th of each month; b) Exergy destruction of the system during the charging stage over an annual cycle.

destruction values between 58 and 240 kW, with the increase in mass flow rate being the dominant factor. The third stage occurs during the months when the system stores sensible heat after the reaction; in this case, the dominant factor is the same as in the first stage: the reactor temperature. The turbine is analysed during the discharge stage because the process is more critical than during charging. During charging, the turbine flow rate is the minimum mass flow rate; during discharge, it depends on the demand.

Integrating simulation models over an annual cycle (Fig. 7b) under the study conditions provides valuable information about the system's dynamic behavior. Fig. 7b shows that exergy destruction is crucial during the calcination reaction for three reasons. First, it contributes to the process itself, as it is irreversible. Second, it increases the CO_2 mass flow rate, which affects the other components. Third, this increased flow rate can cause the other components to operate outside their rated design conditions. This results in the system's exergy destruction ranging from 700 to 1820 kW.

4.3. Discharging stage (carbonation)

During the discharge stage, several processes affect the system efficiency. This section analyses these processes and the impact of their key parameters when integrated into a real industrial demand. This demand comes from a digester for animal lipid generation, which uses waste

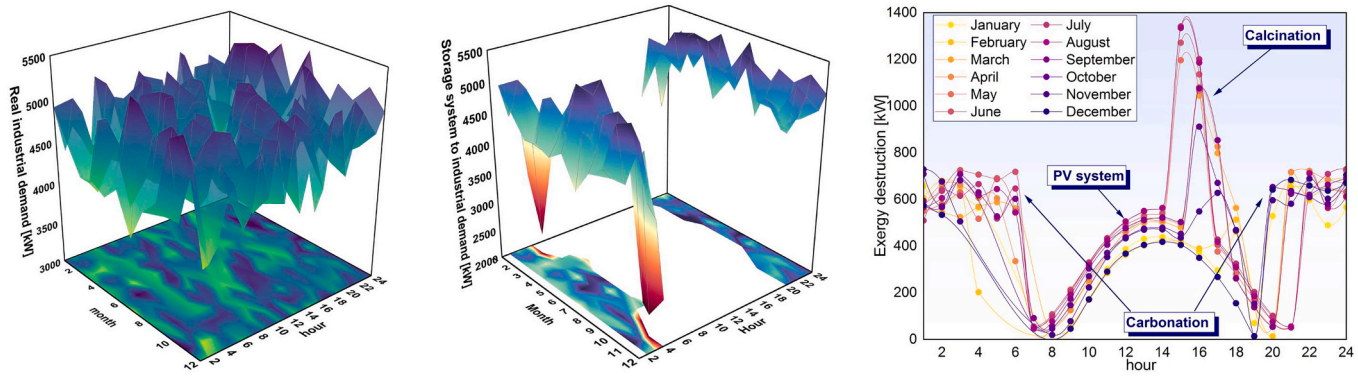


Fig. 8. a) Real industrial demand over an annual cycle; b) Contribution of the storage system to the industrial demand; c) Energy destruction on the 15th of each month, including the charging and discharging stages.

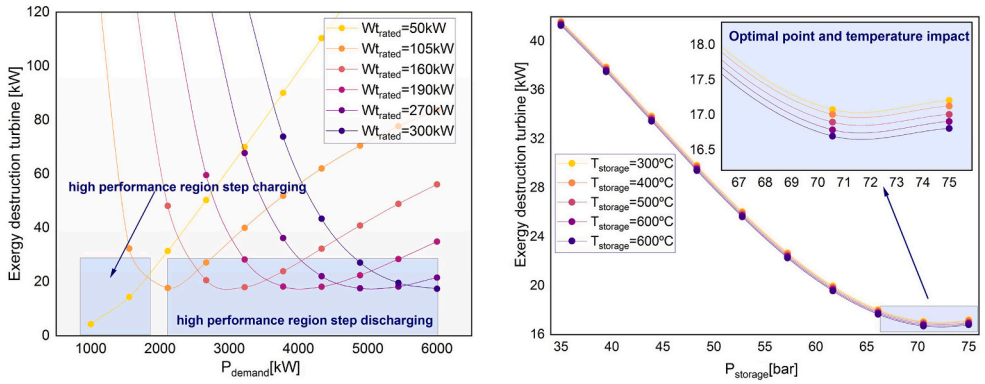


Fig. 9. a) Impact of discharge power on exergy destruction for different turbine rated power, T2. b) Impact of storage pressure on exergy destruction for different storage temperatures.

from the meat industry for biodiesel production. This process incorporates saturated steam at 8 bar, and the real demand was supplied by a waste management company located in Spain. The average thermal demand data from this work coincide with those from this study [71] for animal waste valorisation. Fig. 8a shows the industrial demand over an annual cycle. Fig. 8b shows the contribution of the storage system to the industrial demand over an annual cycle. Fig. 8c shows the system exergy destruction profile on the 15th of each month, including the charging and discharging stage.

Fig. 8a shows the variable behavior of industrial demand for biofuel generation. Demand fluctuates between 3650 and 5380 kW, requiring the storage system to adapt to demand as long as energy is available. Fig. 8b shows the storage system's contribution to demand, which depends on the energy stored during the day and the discharge rate. Specifically, the storage system's discharge time varies between 8:00 PM and 4:00 AM during the winter months and between 9:00 PM and 7:00 AM in months such as July and August. Lower values are also observed between 4:00 AM and 7:00 AM in months such as February and December, because the storage system can no longer meet the entire energy demand. Fig. 8c shows the system's exergy destruction profile. Unlike Fig. 3a, Fig. 8c shows the exergy destruction during the discharge stage, which varies between 400 and 920 kW, depending on the demand. Exergy destruction during the discharge stage varies within a narrower range. The maximum values are lower, and the minimum values are higher because the reaction occurs in a controlled manner to meet the energy demand, unlike what happens during the charging stage.

4.3.1. Turbine

In the discharging stage, the compressed and stored carbon dioxide is expanded to recover energy while its pressure decreases before entering the reactor. This stream has been preheated by the heat exchanger at the storage outlet. These factors make the storage pressure, turbine inlet temperature, reactor pressure, and discharge power the key parameters. In this sense, a scenario similar to compression is presented, where a turbine cannot handle the entire operating range of the mass flow rate under off-design conditions (Fig. 9a).

During the discharge phase, the demand generates power outputs of 3500–5500 kW, resulting in CO_2 mass flow rates of 0.76–1.96 kg/s. Furthermore, the system must manage the minimum CO_2 mass flow rate required to promote bubbling. Fig. 9a shows that operating with only one turbine can lead to significant energy losses and system instability. The adaptive expansion strategy involves a smaller first turbine (T1) with a system-compatible pressure ratio of 75:1, operating at a minimum mass flow rate, with a nominal power of approximately 40 kW and an efficiency of 90%. The second turbine (T2) was selected to minimize exergy destruction during the discharge stage. The optimisation was performed by integrating simulation models over an annual cycle, under the considered conditions and the operating conditions developed by [14]. The turbine's nominal power that minimizes exergy destruction is 190 kW, with off-design efficiencies of between 78 and 90% when operating at a pressure ratio of 75:1. Fig. 9b shows that the system's exergy destruction has an optimal value with respect to the storage pressure, which is close to the pressure proposed in Ref. [15]. The effect of temperature is not critical in this process, indicating that it does not significantly affect exergy destruction. In addition, the turbine inlet temperature depends on the system integration.

4.3.2. Carbonation

The assumptions considered in this work (section 2) imply a temperature range for the solids stored in the reactor of 400 to 875 °C. The solids react with the CO_2 from the turbine, releasing the stored latent heat. Additionally, saturated steam (8 bar under the studied conditions) is generated at this stage to meet industrial demand. These conditions imply that the exergy destruction at this stage depends on the inlet CO_2 temperature, the reactor temperature, the steam pressure (P_{steam}), and the demand. Fig. 10 illustrates the impact of these key parameters on carbonation.

Fig. 10a shows that the temperature increase intensifies operating conditions and moves the process away from the reference state, thus increasing exergy destruction. This can reach up to 600 kW, depending on the discharge power, due to an increase in the mass flow rate handled, regardless of the steam conditions, resulting in a similar impact to the presented in [45]. Fig. 10b shows that the impact of steam pressure is the opposite of that of reactor temperature, a normal effect due to the shape of the isobars on an H-S diagram. It can be observed that exergy destruction decreases as steam pressure increases, making it less critical for lower power outputs. In this respect, this work studies integration based on actual demand, which implies that the steam pressure is imposed. The temperature of the CO_2 entering the reactor (Fig. 10c) has a similar impact to the reactor temperature, although it is less significant. This temperature also moves the system away from the reference state, increasing exergy destruction. Therefore, the proposed system leads to improvements, as the expansion strategy increases isentropic efficiency, thereby decreasing the temperature.

4.4. Annual exergy balance

Fig. 11a (Sankey diagram) shows an annual system exergy destruction of 3656 MWh/year, resulting in an exergy efficiency of 77.8% [72]. This differs from systems that integrate solar energy and CaL. Specifically, the exergy efficiency is nearly double that of the CSP and ORC system in Ref. [45], largely because that system converts solar energy into high-temperature heat using CSP, which destroys more exergy.

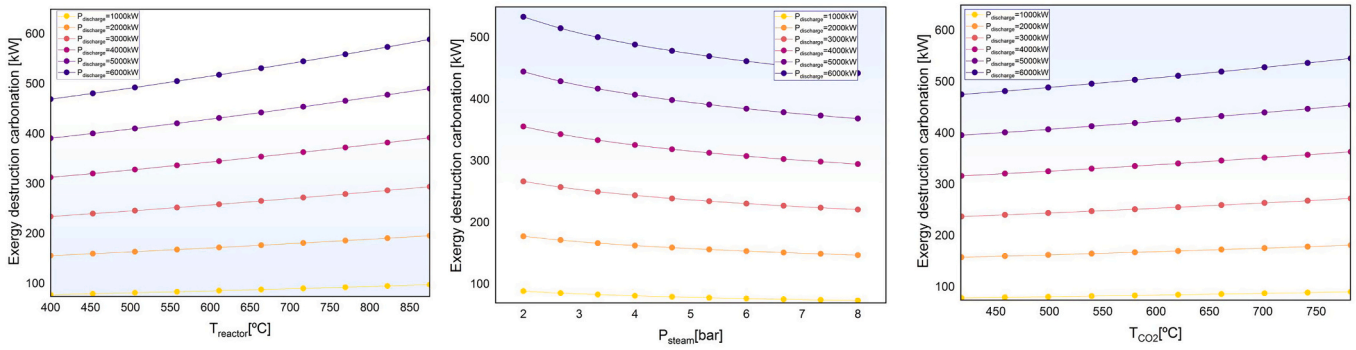


Fig. 10. Impact of key process parameters on exergy destruction during carbonation. a) Impact of reactor temperature for different discharge powers; b) Impact of reactor temperature for different discharge powers; c) Impact of CO_2 inlet temperature for different discharge powers.

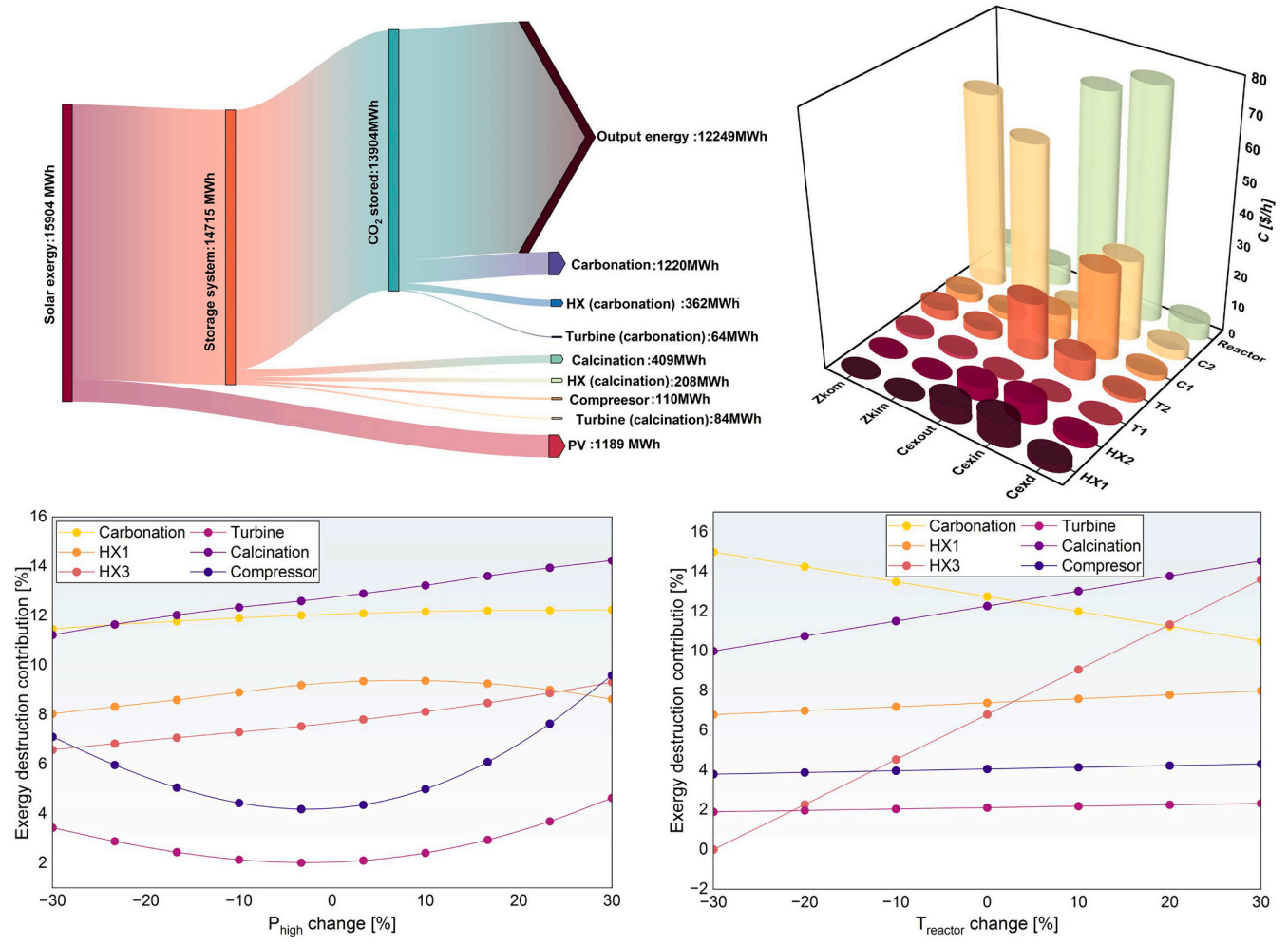


Fig. 11. a) Sankey diagram of exergy destruction [MWh] based on one year of operation; b) Exergoeconomic cost rates; c) Effect of storage pressure (P_{high}) on the exergy destruction distribution among different system components; d) Effect of reactor temperature ($Tr_{reactor}$) on the exergy destruction distribution among different system components.

Compared to Ref. [44], the exergy efficiency in this work is 56% higher due to different system integrations and assumptions. Furthermore, our system shows a 20% improvement over the baseline CSP solar system, and a 14.6% improvement in transport and storage alone, achieved by using a single reactor and an isothermal storage tank. Finally, the power cycle exhibits 24% greater efficiency thanks to a simpler configuration and an optimized compression/expansion strategy.

During the charging step, exergy destruction is 1581 MWh/year, corresponding to an exergy efficiency of 90%. During sunlight hours, the process with the highest exergy destruction is calcination 409 MWh/year, excluding the PV system, while the turbine destroys the least, 64 MWh/year. During the discharging step, exergy destruction reaches 2075 MWh/year with an exergy performance of 85.24%. Here, carbonation accounts for the highest total exergy destruction (220

MWh/year). However, since steam generation accounts for 57% of this, the actual exergy destruction from the carbonation reaction itself is only 524 MWh/year. At night, the turbine remains the component with the lowest exergy destruction (84 MWh/year), a metric that was improved in this work through a multi-turbine operation strategy.

Fig. 11c and d show the exergy destruction behavior as a function of the two most important design parameters: storage pressure (P_{high}) and reaction temperature ($T_{reactor}$), which is linked to the reaction pressure (P_{low}). In this regard, it can be observed that increasing the storage pressure leads to a linear increase in the different system components, in accordance with the fundamental exergy destruction equation, due to operating under harsher conditions. Turbomachinery exhibits a different behavior, as it involves two combined contributions: an increase in temperature and off-design operation. This results in a contribution ranging from 4.4% to 8.2% for the compressor, and from 2.2% to 4.1% for the turbine, with an optimal point close to rated conditions. Regarding the heat exchangers, they also show a distinct behavior with respect to P_{high} due to opposing effects that reduce and increase the area between the temperature lines in the T-Q diagram. This impacts exergy destruction, causing their contribution to vary between 6.1% and 8.2%. For the reactions, this pressure increases the exergy linearly, reaching up to 13.9% for calcination and up to 11.3% for carbonation. In the case of $T_{reactor}$, the behavior is linear for all elements, including turbomachinery, due to a lower weight of this variable on off-design operation. It can be observed that all contributions increase with this temperature, except for carbonation. This is because the thermal gap between the inlet and outlet streams is reduced, resulting in a more efficient heat transfer with a lower thermal gradient (finite temperature difference).

Under the conditions considered, the carbonation and steam generation processes account for 31.2% of the exergy destruction, while the carbonation value stands at 12.1%. The other most critical processes are calcination and the nighttime heat exchanger operation, with values of 12.8% and 9.2%, respectively. The obtained results demonstrate the importance of proper system integration: of the total exergy destruction, only 24.9% is attributed to chemical reactions, whereas 75.1% stems from turbomachinery, heat exchangers, and PV systems.

The exergy balance reveals a diurnal/nocturnal dependency driven by the physical processes occurring between these two periods. During the daytime (charging stage), the system undergoes a reaction that takes place over a shorter, uncontrolled time frame dependent on solar radiation. This scenario leads to an extended period where the system operates at minimum mass flow, with a minor impact on off-design conditions. However, when the reaction takes place, it sharply increases the exergy destruction in components such as the compressor, reactor, and even the heat exchangers, due to variations in the area created by the temperature profile on the T-Q diagram. At night (discharging stage), the power profile is more stable, albeit varying hourly; this leads to a more controlled discharge and better system design, as the mass flow rate managed by the system is more regulated. Nevertheless, during this stage, steam generation based on process demand has been shown to exhibit significant exergy destruction. There are also pronounced differences between summer and winter. During the summer charging stage, reaction conditions are reached during hours of peak radiation, which implies conditions that deviate sharply from rated conditions, making operation more critical for components like the compressor or turbine. Furthermore, the calcination reaction operates under more severe conditions, leading to higher peaks. In the discharging stage, there are no major differences because its conditions are dictated by the demand profile rather than the solar profile, although this stage is prolonged in time due to the greater amount of stored energy.

Table 2
Exergoeconomic data.

Equipment	Z_{KIM}	Z_{KOM}	Operating hour	Rated operating hour	$E_{d,k}$
Units	[$]	[$/year]	[h/year]	[h/year]	[MWh/year]
C1	173,825	10,429	4020	4020	30.5
C2	790,204	47,412	750	62	79.5
T1	82,623	4957	4020	4020	63.7
T2	231,177	13,870	3660	508	362
Reactor	1,210,146	72,608	7680	–	1629
HX1	17,876	1072	4770	580	347
HX2	15,220	913	3660	1781	249

4.5. Exergoeconomic analysis

Exergoeconomic analysis is based on the principles of exergy and economic analysis at the level of system components. Calculating the exergy cost per unit of product streams by revealing the cost-formation process is the primary purpose of an exergoeconomic analysis. To conduct this analysis, it is necessary to apply a cost-benefit equation to each component of the storage system.

The cost balance equation for a system component can be expressed as follows:

$$\sum \dot{C}_{Exout,k} + \dot{C}_{W,k} = \sum \dot{C}_{Exin,k} + \dot{C}_{Q,k} + \dot{Z}_k \tag{33}$$

In exergoeconomic analysis, $\dot{C}_{Exout,k}$ and $\dot{C}_{Exin,k}$ [$/h] are the cost rates of the product and fuel exergy for component k, respectively, based on the exergy of the inlet and outlet material streams of element k. $\dot{C}_{W,k}$ [$/h] is the cost rate associated with the mechanical work entering or leaving component k, $\dot{C}_{Q,k}$ [$/h] is the cost rate associated with the heat transfer streams entering or leaving element k, and $\dot{Z}_k$ [$/h] is the cost rate associated with the monetary flow that encompasses both OPEX and CAPEX. The fuel cost has been obtained as a TTF indicator average using 2024 as the reference, and the electricity cost has been obtained from the European Commission as a 2024 average [73] with values of 35 and 120 $/MWh, respectively. Equipment costs were obtained using correlations derived from the literature based on key system parameters [74,75] (see Appendix D). All equipment costs are referenced with respect to the reference year. To update the cost to the year 2024, the Chemical Engineering Plant Cost Index (CEPCI) has been used.

Table 2 presents the exergoeconomic variables for the system's different streams and processes. Z_{kIM} is the CAPEX of the kth component, Z_{kOM} is the annual maintenance costs of the kth component, n_o are the operating hours of the kth component, and $E_{d,k}$ [MWh/year] is the exergy destruction obtained in the previous section.

The integration of simulation models over an annual cycle, accounting for environmental conditions and industry demand, has enabled the determination of the operating hours (no) of each component, leading to a more realistic exergoeconomic analysis. These data have enabled the cost rates of the different elements to be determined, expressed in $/h (Table 3). Where $\dot{Z}_{kIM}$ is the CAPEX cost rate of component k, $\dot{Z}_{kOM}$ is the OPEX cost rate of component k, $\dot{C}_{Exd,k}$ and $\dot{C}_{Exd,k}$ is the exergy destruction cost rate of component k and $\dot{C}_{Exin,k}$ and $\dot{C}_{Exout,k}$ are the cost rates of the input and output exergy of component k, respectively. Fig. 11c shows the cost rates for the system's components.

Fig. 11c summarizes the exergoeconomic study for the set of economic assumptions. The highest values are those of the reactor, mainly the cost rates of input and output exergy, which are 74 and 68.8 $/h, respectively, with CAPEX and OPEX cost rates of $6.90 and $8.28/h, respectively. In the C_1 compressor, it is possible to observe that the input cost rate is much higher than the output cost rate, because the average costs per exergy unit considered is higher; the cost per inlet exergy unit is based on electrical energy and the cost per outlet exergy unit is based on thermal energy, whose values are 0.12 and 0.035$/kWh, respectively. The CAPEX and OPEX cost rates are low because the investment is low and operates for many hours, 4020 h. The C_2 compressor shows

Table 3
Cost rates.

Equipment	$\dot{Z}_{k_{IM}}$	$\dot{Z}_{k_{OM}}$	$\dot{C}_{Exd,k}$	$\dot{C}_{Exin,k}$	$\dot{C}_{Exout,k}$
Units	[$/h]	[$/h]	[$/h]	[$/h]	[$/h]
C1	2.16	2.59	1.76	28.70	8.36
C2	52.68	63.21	3.48	26.18	4.15
T1	0.83	1.23	0.042	0.164	0.41
T2	2.89	3.47	1.30	6.70	18.43
Reactor	6.90	8.28	5.61	74	68.8
HX1	0.18	0.22	2.54	7.85	5.43
HX2	0.19	0.23	2.19	6.69	4.50

higher CAPEX and maintenance costs because its investment is much higher than that of the C1, and it operates for only 750 h. It can be observed that integrating a second optimized compressor improves performance, as its exergy destruction cost rate is similar to that of compressor C_1, even when operating with a variable mass flow rate. In turbines, the situation is the opposite of that in compressors: the average cost per unit of input exergy is higher than that of output exergy. In addition, the exergy destruction cost rates are low based on good integration of the turbines hour-by-hour. The CAPEX and OPEX cost rates for turbine T_2 are less important than those for compressor C_2 because the larger turbine operates overnight, with 3660 h of operation. Both heat exchangers exhibit similar behavior, with low CAPEX and maintenance cost rates. In addition, exergy destruction cost rates are low due to the good integration of the temperature profiles, indicating that these processes are not critical in this study. The exergoeconomic analysis yields a levelized storage cost (LCOS) of approximately $30/MWh and destruction cost rates of $10.7 and $6.1/h for charging and discharging, respectively, reaching an average annual value of $6.35/MWh. Assuming a useful life of 30 years, the payback period is 17.8 years, with an LCOE, including the PV system, of $76.21/MWh, which is consistent with other works [41] that integrate solar energy based on CaL and even with works with different approaches [41,76]. These results indicate that these systems may represent an opportunity for medium-scale industrial implementation.

4.5.1. Economic analysis

The exergoeconomic results presented above are based on a single set of economic assumptions, such as CAPEX for system components obtained through correlations and a specific electricity or gas price. While this is a reasonable starting point, the conclusions regarding competitiveness are quite sensitive to these assumptions. Therefore, a sensitivity analysis of storage costs and the levelized cost of energy (LCOE) was performed with respect to key economic parameters. This sensitivity analysis examines the impact of ±30% variations in CAPEX and fuel and electricity prices. Fig. 12 shows the impact of CAPEX, fuel, electricity prices and maximum carbonation conversion when they vary between −30 and 30% on the LCOE and LCOS.

Fig. 12a shows that CAPEX variations have a significant impact on the LCOS and LCOE. These variations can significantly alter the system's energy viability, potentially increasing the LCOE by 33.3% and the LCOS by 6.7%. Furthermore, the figure shows that a decrease in technology costs, for example, due to manufacturing improvements, could increase the system's viability by up to 22% relative to the LCOE. In this respect, the LCOE is more critical because CAPEX variations affect the photovoltaic system, whose CAPEX is almost seven times that of the storage system, assuming a photovoltaic installation price of $1/Wp, consistent with other similar studies. Changes in OPEX are generally less critical than changes in CAPEX because their contribution to total costs is less significant, and they are even less critical to the LCOE due to the high CAPEX contribution of the photovoltaic system. Fig. 12b shows that the fuel price could reduce the system's energy viability by up to 11% relative to the LCOS and by up to 2% relative to the LCOE. The electricity

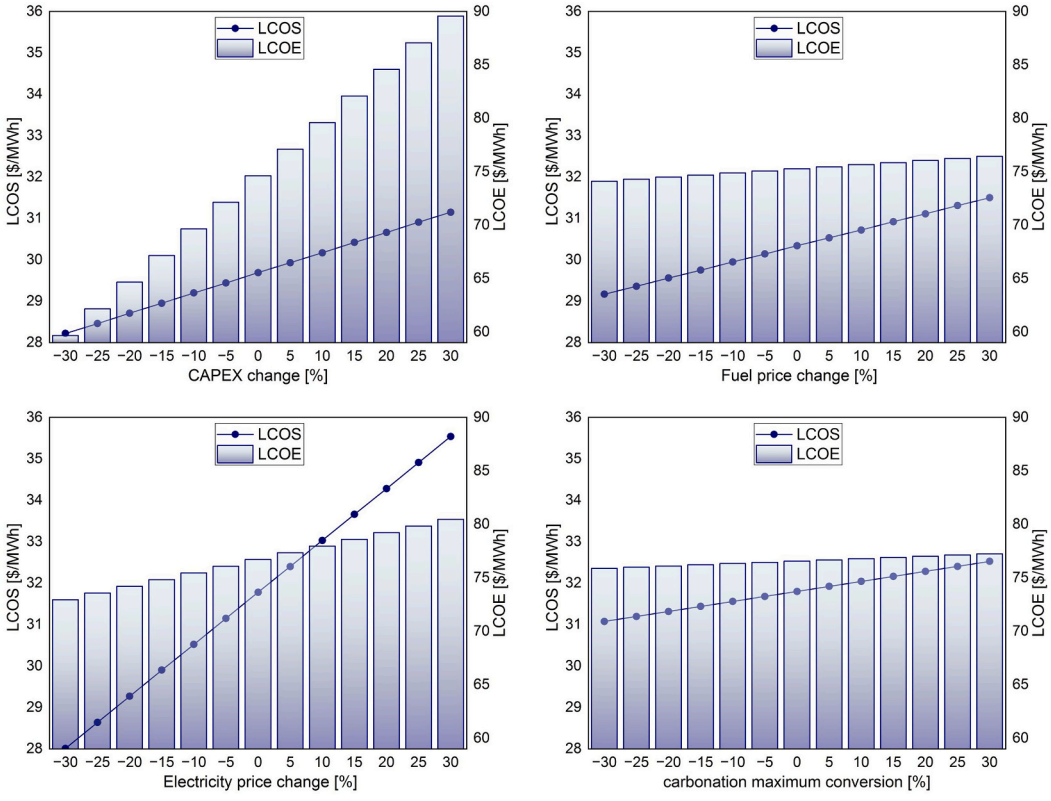


Fig. 12. Impact of economic parameters and carbonation maximum conversion on LCOS and LCOE. a) CAPEX; b) Fuel price; c) Electricity price; d) carbonation maximum conversion.

price can have a more significant overall impact than the fuel price due to higher electricity consumption and prices, potentially leading to a decrease in system viability of up to 4.75% relative to the LCOE and 32% relative to the LCOS (Fig. 12c). Fig. 12d shows that the impact of the maximum carbonation conversion on the LCOE and LCOS is not significant compared to the CAPEX. This is logical, as its contribution to the CAPEX varies between 17% and 31% depending on the maximum carbonation conversion, which has a direct impact on the reactor's CAPEX and the limestone mass, in addition to modifying its OPEX. Even so, a variation in the carbonation rate between 30% and 30% produces an LCOE modification of up to 4.15%, showing a similar trend for the LCOS. Overall, it is shown that the maximum carbonation conversion does not have a major impact on costs, as it affects CAPEX acquisition but has little impact on system performance, which is consistent with other studies [57].

5. Conclusions

The increase in renewable energy generation, driven by cost reductions, has increased the economic viability of these systems, which now face the challenge of improving their integration. Integrating photovoltaic systems with advanced storage systems could be fundamental to decarbonise existing industrial processes. TCES based on CaL represent a promising alternative that could improve the current situation and should be studied in depth under off-design conditions to achieve greater acceptance. This paper presents an exergy and exergoeconomic study of a modular CaL. The integration study is based on real industrial demand over an annual cycle when the system is integrated into a biofuel generation process, providing a more realistic scenario under off-design conditions. The system employs an adaptive compression/expansion strategy to mitigate fluctuations and improve efficiency.

The annual exergy study shows that the most critical key parameters are reactor temperature and pressure, as well as storage temperature and pressure. In general, increases in these parameters lead to more severe conditions that move the system further from the reference state, thus increasing exergy destruction. In the charging step, photovoltaic power has a significant impact, as it increases the reactor temperature if reaction conditions have not yet been reached, and it increases the mass flow rate through the system once they are. The annual off-design study shows that the compressor often operates under unstable conditions, resulting in unacceptable exergy losses, making it the most critical component. This work proposes an adaptive compression strategy that increases flexibility by using two compressors. This strategy demonstrates its ability to adapt to off-design conditions under real industrial demand. The smaller compressor is correctly adjusted to the mass flow rate before the reaction, while the larger, optimized compressor adjusts to the mass flow rates once the reaction conditions are reached. The expansion process leads to a scenario similar to compression when integrated with actual industrial demand. However, it is less critical because the enthalpy drop is smaller and the variations in discharge rate are less significant. This work also proposes an adaptive expansion strategy, comprising a turbine that adapts to the mass flow rate during charging and another that optimises exergy destruction during discharging. These measures significantly optimise integration into an industrial process, achieving an overall exergy efficiency of 77.8%, with an annual contribution to exergy destruction of 4.2% and 4.5% for compression and expansion, respectively. This scenario makes the reactor the most critical component of the storage system, with exergy destruction of 12.1% and 12.8% for carbonation and calcination, respectively, followed by heat exchangers, which account for 7.5% and 9.2% for calcination and carbonation, respectively. Steam generation has been shown to have a significant impact on total exergy destruction, accounting for 19.1%, but this impact depends on the industrial process rather than the storage system.

The exhaustive study of the system's exergy has enabled a corresponding exergoeconomic study that accounts for the operating hours of the different components and their contributions to cost rates, leading to more accurate results. The results show that the reactor is the most critical element, with a cost rate based on exergy destruction of $5.6 per hour of operation. The highest capital investment and operating and maintenance costs correspond to the larger compressor, due to its limited operating hours, reaching $116 per operating hour, compared to the turbine, which has a cost of $6.40 per operating hour due to a considerable increase in operating hours. In general terms and under the set of economic assumptions considered as a starting point, the exergoeconomic analysis also shows good integration, resulting in competitive values compared to current technologies, yielding a value of $30 per MWh stored with cost rates based on exergy destruction of $6.35 $/MWh and an LCOE of $76.21 per MWh generated, including the photovoltaic system. Sensitivity analysis indicates that the system's LCOE could experience percentage variations ranging from −22% to 33%, depending on the CAPEX of the integrated technologies and the maximum conversion considered, although the latter has not shown a very significant impact on LCOE. The LCOS also shows fluctuations, leading to variations between −5.3% and 10.2% for CAPEX, and up to 1.8% with respect to the maximum conversion considered. Fluctuations in electricity and fuel prices also have a significant impact, causing increases of up to 32% and 4.7% in LCOE and LCOS, respectively. In light of these results, specialized studies are proposed on reactor conditions or the integration of turbomachinery, depending on the process, to reduce costs and increase overall efficiency.

The present study validates the practical application of our current laboratory-scale research through a modular, container-based scheme, demonstrating robust scalability and direct benefits for industrial modernization. By facilitating off-site manufacturing and plug-and-play deployment, this modular approach minimizes plant downtime. Exergoeconomic analysis yields a realistic return on investment that can be further improved through economies of scale, advanced manufacturing techniques, and cost reductions driven by technological maturity. Furthermore, the inherent flexibility of the containerized design ensures high compatibility with continuously evolving regional energy and environmental policies, positioning it as a highly adaptable solution for industrial decarbonization and circular energy transitions.

CRediT authorship contribution statement

J.M. Guisado: Methodology, Investigation, Formal analysis, Conceptualization. **C. Ortiz:** Validation, Resources, Conceptualization. **J.A. Becerra:** Visualization, Project administration. **A. Marques-Valderrama:** Formal analysis, Data curation. **R. Chacartegui:** Supervision.

Declaration of competing interest

The authors declare that they have no known competing financial interests or personal relationships that could have appeared to influence the work reported in this paper.

Acknowledgement

This work was partially funded from the EU Next Generation Funds and from the Spanish Ministry of Science and Innovation, through the projects ‘HIPERTES: Procesos y componentes para el almacenamiento híbrido de energía térmica basado en sales fundidas y carbonatos’, grant PID2022-140815OB-C21 and the project ‘METHCESFUEL: Renewable Methanol-based Synthetic Multifuel Production’ from the European Commission through Horizon, the EU Framework Programme for Research and Innovation, under Grant Agreement No. 101235215.

Appendices

Appendix A: P_r model

The P_r parameter depends on the environmental conditions and characteristics of the solar photovoltaic panel

$$P_r\ [-] = \frac{G_{POA}}{G_{cell_{STC}} \bullet \left(1 - \frac{\beta}{100}\left(T_{cell} - T_{cell_{STC}}\right)\right)} \tag{A.1}$$

where T_{cell} and $T_{cell_{STC}}$ $[^{\circ}C]$ are the temperature of the cell in the period and the temperature of the reference cell, G_{POA} $[W/m^2]$ and $G_{cellTSC}$ $[W/m^2]$ are global irradiance in the plane of the PV panel and reference global irradiance in the plane of the PV panel, and β $[\%/^{\circ}C]$ is the coefficient of power variation with temperature.

The temperature of the panel can be calculated as a function of the ambient temperature from Eq. A.2, which has been used in other works [58]:

$$T_{cell}\ [^{\circ}C] = T_a + \frac{NOCT - T_{ref}}{G_{refc}} G_{POA} \tag{A.2}$$

where NOCT (°C), T_a and T_{ref} (°C) are the operational temperature of the cell, ambient temperature and reference ambient temperature of the cell, respectively; G_{refc} $[W/m^2]$ are irradiance reference NOCT and irradiance. The reference values have been supplied by a manufacturer of photovoltaic panels, NOCT $= 47^{\circ}C, \beta = 0.33\%/^{\circ}C$, $T_{ref} = 25^{\circ}C$, $G_{refc} = 800\ W/m^2$, and $A_{PV} = 1.94 m^2$.

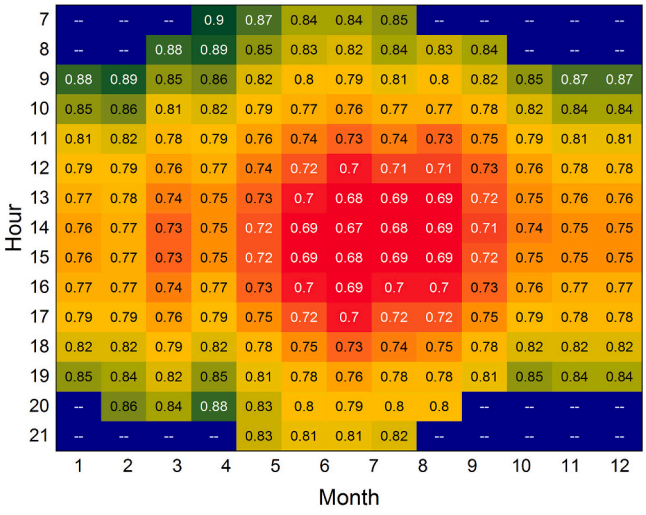


Fig. A.1. Average hourly P_r values during an annual cycle.

Appendix B: Kinetic reaction

In the literature, some models describe carbonation behavior. In this work, the carbonation reaction is defined in Eqs. (B.1)–(B.3) [35], which defines the relationship between equilibrium pressure (P_{equi}) and reaction temperature(T).

$$r\left(T, P_{equi}\right) \approx a \bullet e^{-\frac{\Delta S_0^2}{R_e} - \frac{E_1}{RT}} \cdot \left(\frac{P}{P_{equi}} - 1\right) \tag{B.1}$$

$$P_{equi} = 4.083 x 10^7 \bullet e^{-20{,}474/T} \tag{B.2}$$

$$\frac{dx}{dt} = X\left(1 - \frac{x}{x_{max}}\right) r(T, P) \longleftrightarrow x(t) = \frac{x_{max}}{1 + e^{-r(t - t_0)}} \tag{B.3}$$

E_1 (180kJ/mol) is the carbonation activation energy, a2 is a preexponential factor, and R is the gas constant. The Van't Hoff equation has been used for the equilibrium constant, being ΔS_0^2 standard free energy change of carbonation (−68 J/mol·K). x_{max} is the maximum CaO conversion limit, set to 0.15 in this study, since we assume there is no solid make-up and that carbonation during the diffusive stage is negligible under the proposed reactor conditions [15,35].

Appendix C: Off-design conditions

C.1. Compressor

$$R_{r_c}[-] = c_1(n_{r_c}) + c_2 G_c + c_3(n_{rc}) \tag{C.1}$$

$$\eta_{rc}[-] = \left(1 - c_4(1 - n_{r_c})^2\right)\left(\frac{n_{rc}}{G_c}\right)\left(2 - \frac{n_{r_c}}{G_c}\right) \tag{C.2}$$

$$c_1 = \frac{n_{c_r}}{p(1 - mn_{rc}) + n_c(n_{r_c} - m)^2}; c_2 = \frac{p - 2mn_{c_r}}{p(1 - mn_{rc}) + n_c(n_{r_c} - m)^2}; c_3 = \frac{pmn_{c_r} - m^2 n_{c_r}^3}{p(1 - mn_{rc}) + n_c(n_{r_c} - m)^2}; c_4 = 0.3 \tag{C.3}$$

$$G_{rc} = \frac{G_c}{G_d}; G_c = \frac{m_c\sqrt{RT_{c,in}}}{D^2 P_{c,in}\sqrt{\gamma}}; G_d = \frac{m_d\sqrt{RT_{c,in_d}}}{D^2 P_{c,in_d}\sqrt{\gamma_d}} \tag{C.4}$$

$$n_{r_c} = \frac{n_c}{n_d}; n_c = \frac{N_c \bullet D}{a}; n_d = \frac{N_d \bullet D}{a_d} \tag{C.5}$$

$$R_{r_c} = R_c/R_d \tag{C.6}$$

$$\eta_{rc} = \eta_c/\eta_d \tag{C.7}$$

where $\eta_{r_c}, R_{r_c}, n_{r_c}$ and G_{r_c} is the relative efficiency [−], the relative compression ratio [−], the relative rotational speed and the relative dimensionless flow rate [−], respectively, m_c[kg/s] is the mass flow rate of CO_2 in the system. N_c and N_d are the rotation speed and rotational speed under rated conditions, D is the diameter of the turbomachinery; a and a_d are the speed of sound and the speed of sound under rated conditions; γ is the heat capacity ratio of air; $P_{c,in}$, $T_{c,in}$, P_{c,in_d} and T_{c,in_d} are the temperatures and pressures at the compressor inlet in off-design and rated design, respectively. The variables m and p are associated with the curve shape, which in this specific case are equal to 1.8 for both constants [64,77], taking into account the use of a centrifugal compressor, which is also consistent with similar studies that have utilized CO_2 [9,78].

At a certain rotational speed, a surge occurs in the compressor when the mass flow rate is below a threshold. The mass flow rate should be higher than the limiting mass flow rate at the surge point to avoid the compressor operating in unstable conditions. Under the rated rotational speed, surge margin can be calculated according to the following equations [64,77]:

$$\text{Surge margin}[\%] = ((R_{cs}/G_{cs})/(R_d/G_d) - 1) \bullet 100 \tag{C.8}$$

where the subscript *s* denotes the surge point.

Under other off-design rotational speeds, the isentropic efficiency at the surge point is calculated from the following equation:

$$\eta_{c_{SM}=1-a(1-N_c)^2} \tag{C.9}$$

where $\eta_{c_{SM}}$ is based on the isentropic efficiency of the surge point at rated rotational speed, where the value of a is taken as 0.7 based on experimental data fitting and used in similar works [79].

C.2. Turbine

$$G_{r_T}[-] = \sqrt{1.4 - 0.4n_{r_T}}\sqrt{\frac{\frac{1}{\beta_T^2} - 1}{\frac{1}{\beta_d^2} - 1}} \tag{C.10}$$

$$\eta_{r_T}[-] = \frac{\eta_T}{\eta_d} = \left(1 - t_4(1 - n_{r_T})^2(n_{r_T} - G_c)\left(2 - \frac{n_{r_T}}{G_c}\right)\right. \tag{C.11}$$

$$G_{r_T}[-] = \frac{G_T}{G_d}; G_T = \frac{m_c\sqrt{RT_{T,in}}}{D^2 P_{T,in}\sqrt{\gamma}}; G_d = \frac{m_d\sqrt{RT_{T,in_d}}}{D^2 P_{T,ind}\sqrt{\gamma_d}} \tag{C.12}$$

$$\beta_{r_T} = \beta_T/\beta_d \tag{C.13}$$

$$\eta_{r_T} = \eta_T/\eta_d \tag{C.14}$$

$$n_{r_T} = \frac{n_T}{n_d}; n_e = \frac{N_T \bullet D}{a}; n_d = \frac{N_d \bullet D}{a_d} \tag{C.15}$$

where $\eta_{r_T}, R_{r_T}, n_{r_T}$ and G_{r_T} are the relative performance [−], relative compression ratio [−], relative rotational speed and relative dimensionless mass flow rate [−], respectively, which have been used in other works [42]. $T_{T,in}$ and T_{T,in_d} are the input temperatures in the expansion process in off-design and rated considerations, respectively; $P_{T,in}$ and P_{T,in_d} are the input pressures in the expansion process in off-design and rated considerations, respectively; β_T and β_d are the ratio pressure in the expansion process in off-design and rated considerations, respectively; T_4 is a constant related to the

turbine map type, which is assumed to be 0.3. This value is supported by literature [64,77] as validated for off-design operations, even under conditions similar to those in CO_2-based systems [8,9].

C.3. Off-design model validation

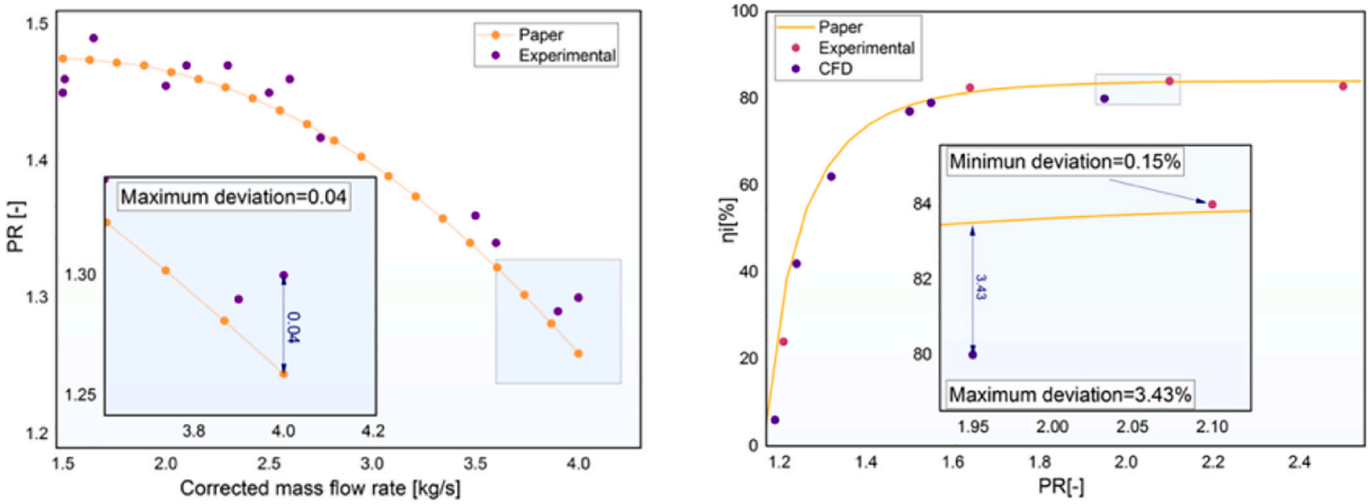


Fig. C.1. Off-design model accuracy evaluation (left: compressor; right: turbine).

The off-design turbine model has been validated using experimental data from this work [69] and the CFD model developed by Salah [43]. Fig. C.1 demonstrates that the off-design turbomachinery model is suitable for this study. For the compressor, the maximum deviation in the pressure ratio occurs at a mass flow rate of approximately 4 kg/s, reaching 3%. In the turbine, the maximum deviation is observed in the isentropic efficiency, reaching 3.43% at a pressure ratio of 1.95. The mean deviations are 2.17% for the compressor model and 1.86% for the turbine. These accuracies confirm the models are valid; in the worst-case scenario, results may deviate by up to 3.4%, a margin accounted for in this study. The isentropic efficiency of compressor C_2 reaches 76% at 70% of the nominal flow rate, dropping to 50% at 50% flow, and peaks at 87% under rated conditions. Similarly, turbine T_2 achieves an isentropic efficiency of nearly 79% at 70% nominal flow, decreases at 50% flow, and reaches 90% at rated conditions.

Appendix D: Exergoeconomic analysis

Eq. (33) can be expressed in terms of the unit costs assigned to each flow (Eq. (D.1)).

$$\sum E_{Exout,k} \bullet C_{out,k} + C_{W,k} \bullet W = \sum E_{Ein,k} \bullet C_{in,k} + C_{Q,k} \bullet Q + \dot{Z}_k \tag{D.1}$$

where $C_{out,k}$, $C_{in,k}$, $C_{W,k}$ and $C_{Q,k}$ are the average costs per exergy unit, $/GJ.

The cost rate associated with the capital investment, operation and maintenance for the kth component can be expressed as follows.

$$\dot{Z}_k = \dot{Z}_{k_{IM}} + \dot{Z}_{k_{OM}} \tag{D.2}$$

where $\dot{Z}_{k_{IM}}$ is the annual levelized capital investment, and $\dot{Z}_{k_{OM}}$ is the annual levelized operating and maintenance cost. They are shown in Table 3, which also shows the economic data and the cost functions.

Values of the exergoeconomic factor (f_k) and the relative cost difference (r_k) for the kth component can be expressed respectively as

$$f_k = \frac{\dot{C}_{P,k} - \dot{C}_{F,k}}{\dot{C}_{F,k}} \tag{D.3}$$

$$r_k = \frac{\dot{Z}_k}{\dot{Z}_k + \dot{C}_{D,k}} \tag{D.4}$$

where $\dot{C}_{D,k}$, $\dot{C}_{F,k}$ and $\dot{C}_{P,k}$ are the cost rate associated with the exergy destruction of $E_{F,K}$, $E_{P,K}$ and $E_{D,K}$.

Table D.1
Economic data and the cost functions.

Equipment	Correlation [$]	Equipment Coefficients	Reference year	Reference
Reactor	$15594 \bullet Q_{carbonation}(kW)^{0.5}$	5442 kW	2016	[74]
Turbines	$8279 \bullet W_{T_2}^{0.684}$	40 kW(T1); 190 kW(T2)	2013	[75]
Compressors	$7331 \bullet W_{compressor}(kW)^{0.7865}$	56 kW(C1); 292 kW(C2)	2003	[75]
Heat exchanger	$32.3 \bullet Q_{HX}(kW)$	346 kW(HX1); 301 kW(HX2)	2017	[75]

(*continued on next page*)

Table D.1 (*continued*)

Equipment	Correlation [$]	Equipment Coefficients	Reference year	Reference
Limestone	$m_{CaCO_3} \bullet C_{CaCO_3}$	1300 t ($C_{CaCO3} = 10\$/t$)	2019	[80]
Reservoir	$23400 \bullet V(m^3)$	130 m^3	2022	[15]

Table D.2
Economic data.

Economic data		Reference
Lifetime, *n*	20	[81]
Annual operation hours	8760	[82]
Interest rate	12%	[83]
Capital recovery factor	$i_r(1+i_r)^n/((1+i_r)^n-1)$	[84]
Discount rate	10%	[15]
Maintenance factor	6%/year	[83]
Cost fuel	35$/MWh (2024)	[73]
Cost Electricity	120$/MWh (2024)	[73]

All equipment costs are referenced to the base year. To update the cost to 2024, the Chemical Engineering Plant Cost Index (CEPCI) is applied, which has an annual average value of 800.2 [85], Eq. (D.5).

$$C_{2024} = C_{ref}\left(\frac{CEPCI_{2024}}{CEPCI_{ref}}\right) \tag{D.5}$$

Data availability

Data will be made available on request.

References

[1] da Silva JAM, Ávila Filho S, Carvalho M. Assessment of energy and exergy efficiencies in steam generators. J Braz Soc Mech Sci Eng 2017;39(8):3217–26. https://doi.org/10.1007/s40430-016-0704-6.

[2] Leonard MD, Michaelides EE, Michaelides DN. Energy storage needs for the substitution of fossil fuel power plants with renewables. Renew Energy 2020;145:951–62. https://doi.org/10.1016/j.renene.2019.06.066.

[3] Alcañiz A, Grzebyk D, Ziar H, Isabella O. Trends and gaps in photovoltaic power forecasting with machine learning. Elsevier Ltd; 2023. https://doi.org/10.1016/j.egyr.2022.11.208.

[4] "JRC135034_01".

[5] "REPowerEU - 3 years on." Accessed: Apr. 14, 2026. [Online]. Available: https://energy.ec.europa.eu/topics/markets-and-consumers/actions-and-measures-energy-prices/repowereu-3-years_en.

[6] Tiktas A, Gunerhan H, Hepbasli A, Açıkkalp E. Extended exergy analysis of a novel integrated absorptional cooling system design without utilization of generator for economical and robust provision of higher cooling demands. Energ Conver Manage 2024;307:118350. https://doi.org/10.1016/J.ENCONMAN.2024.118350.

[7] Tiktas A, Hepbasli A. A key review of geothermal heat pumps: exergoeconomic and environmental aspects with prospects for further development. Next Energy 2026;10:100482. https://doi.org/10.1016/J.NXENER.2025.100482.

[8] Guisado JM, Carro A, Chacartegui R. Avoidable exergy performance analysis in the integration of an electrothermal energy system based on transcritical CO2 cycles. Energy Convers Manag 2026;348:120706. https://doi.org/10.1016/j.enconman.2025.120706.

[9] Guisado JM, et al. Analytical investigation of the compressor layout for off-design operation of a transcritical CO2 cycle in an electrothermal energy storage. Energy Convers Manage X 2025;28:101299. https://doi.org/10.1016/j.ecmx.2025.101299.

[10] "IAEA BULL IAEA BULLE ETIN TIN." [Online]. Available: www.iaea.org/bulletin.

[11] Ma X, Du Y, Li B, Li X, Zhang C, Wu Y. Decarbonization planning framework: high-temperature heat pump integration for steam-based industrial parks. Appl Therm Eng 2026;283:128984. https://doi.org/10.1016/J.APPLTHERMALENG.2025.128984.

[12] Jesper M, Pag F, Vajen K, Jordan U. Annual industrial and commercial heat load profiles: modeling based on k-means clustering and regression analysis. Energy Convers Manag X 2021;10:100085. https://doi.org/10.1016/J.ECMX.2021.100085.

[13] Lima RGA, Calili RF, Almeida MFL, Silva FL, Santos S, Velásquez R. Estimating the potential for thermal energy efficiency in the industrial sector: a hybrid model integrating exergy analysis and long-term technology diffusion scenarios. Energy 2024;313:133824. https://doi.org/10.1016/J.ENERGY.2024.133824.

[14] Sciacovelli A, et al. Dynamic simulation of adiabatic compressed air energy storage (A-CAES) plant with integrated thermal storage – link between components performance and plant performance. Appl Energy 2017;185:16–28. https://doi.org/10.1016/J.APENERGY.2016.10.058.

[15] AlShafi M, Bicer Y. Thermodynamic performance comparison of various energy storage systems from source-to-electricity for renewable energy resources. Energy 2021;219. https://doi.org/10.1016/j.energy.2020.119626.

[16] Ortiz C, García-Luna S, Carro A, Carvajal E, Chacartegui R. Techno-economic analysis of a modular thermochemical battery for electricity storage based on calcium-looping. Appl Energy 2024;367. https://doi.org/10.1016/j.apenergy.2024.123366.

[17] Wang K, Yan T, Li RK, Pan WG. A review for ca(OH)2/CaO thermochemical energy storage systems. J Energy Storage 2022;50. https://doi.org/10.1016/j.est.2022.104612.

[18] Walden JVM, Bähr M, Glade A, Gollasch J, Tran AP, Lorenz T. Nonlinear operational optimization of an industrial power-to-heat system with a high temperature heat pump, a thermal energy storage and wind energy. Appl Energy 2023;344. https://doi.org/10.1016/j.apenergy.2023.121247.

[19] Khosa AA, Xu T, Xia BQ, Yan J, Zhao CY. Technological challenges and industrial applications of CaCO3/CaO based thermal energy storage system – a review, Elsevier Ltd; 2019. https://doi.org/10.1016/j.solener.2019.10.003.

[20] Ortiz C, Binotti M, Romano MC, Valverde JM, Chacartegui R. Off-design model of concentrating solar power plant with thermochemical energy storage based on calcium-looping. AIP Conf Proc 2019. https://doi.org/10.1063/1.5117755.

[21] Ortiz C, Valverde JM, Chacartegui R, Perez-Maqueda LA, Giménez P. The calcium-looping ($CaCO_3$/CaO) process for thermochemical energy storage in concentrating solar power plants. Elsevier Ltd; 2019. https://doi.org/10.1016/j.rser.2019.109252.

[22] Carro A, Chacartegui R, Ortiz C, Arcenegui-Troya J, Pérez-Maqueda LA, Becerra JA. Integration of calcium looping and calcium hydroxide thermochemical systems for energy storage and power production in concentrating solar power plants. Energy 2023;283. https://doi.org/10.1016/j.energy.2023.128388.

[23] Raganati F, Ammendola P. Review of carbonate-based systems for thermochemical energy storage for concentrating solar power applications: state-of-the-art and outlook. Energy Fuels 2023;37(3):1777–808. https://doi.org/10.1021/acs.energyfuels.2c03853.

[24] Bogdanovi B, Reiser A, Schlichte K, Spliethoff B, Tesche B. Thermodynamics and dynamics of the Mg-Fe-H system and its potential for thermochemical thermal energy storage. J Alloys Compd 2002;345(1–2):77–89. https://doi.org/10.1016/S0925-8388(02)00308-0.

[25] Møller KT, et al. Complex metal hydrides for hydrogen, thermal and electrochemical energy storage. Energies (Basel) 2017;10(10). https://doi.org/10.3390/en10101645.

[26] Yan T, Wang RZ, Li TX, Wang LW, Fred IT. A review of promising candidate reactions for chemical heat storage. Renew Sustain Energy Rev 2015;43:13–31. https://doi.org/10.1016/j.rser.2014.11.015.

[27] Bagherisereshki E, Tran J, Lei F, AuYeung N. Investigation into SrO/SrCO<inf>3</inf> for high temperature thermochemical energy storage. Sol Energy 2018;160:85–93. https://doi.org/10.1016/j.solener.2017.11.073.

[28] Chacartegui R, Alovisio A, Ortiz C, Valverde JM, Verda V, Becerra JA. Thermochemical energy storage of concentrated solar power by integration of the calcium looping process and a CO_2 power cycle. Appl Energy 2016;173:589–605. https://doi.org/10.1016/j.apenergy.2016.04.053.
[29] Alovisio A, Chacartegui R, Ortiz C, Valverde JM, Verda V. Optimizing the CSP-calcium looping integration for thermochemical energy storage. Energy Convers Manag 2017;136:85–98. https://doi.org/10.1016/j.enconman.2016.12.093.
[30] Fernández R, Ortiz C, Chacartegui R, Valverde JM, Becerra JA. Dispatchability of solar photovoltaics from thermochemical energy storage. Energy Convers Manag 2019;191:237–46. https://doi.org/10.1016/j.enconman.2019.03.074.
[31] Xu Q, Wang L, Li Z, Shi L. A calcium looping system powered by renewable electricity for long-term thermochemical energy storage, residential heat supply and carbon capture. Energ Conver Manage 2023;276. https://doi.org/10.1016/j.enconman.2022.116592.
[32] Abanades JC, Alvarez D. Conversion limits in the reaction of CO_2 with lime. Energy and Fuels 2003;17(2):308–15. https://doi.org/10.1021/ef020152a.
[33] Romeo LM, Lara Y, Lisbona P, Escosa JM. Optimizing make-up flow in a CO_2 capture system using CaO. Chem Eng J 2009;147(2–3):252–8. https://doi.org/10.1016/j.cej.2008.07.010.
[34] Sun H, Li Y, Yan X, Zhao J, Wang Z. Thermochemical energy storage performance of Al_2O_3/CeO_2 co-doped CaO-based material under high carbonation pressure. Appl Energy 2020;263. https://doi.org/10.1016/j.apenergy.2020.114650.
[35] Ozcan DC, Shanks BH, Wheelock TD. Improving the stability of a CaO-based sorbent for CO<inf>2</inf> by thermal pretreatment. Ind Eng Chem Res 2011;50(11):6933–42. https://doi.org/10.1021/ie102368g.
[36] Ortiz C, Valverde JM, Chacartegui R, Perez-Maqueda LA. Carbonation of limestone derived CaO for thermochemical energy storage: from kinetics to process integration in concentrating solar plants. ACS Sustain Chem Eng 2018;6(5):6404–17. https://doi.org/10.1021/acssuschemeng.8b00199.
[37] Marchi B, Zanoni S. Investments in energy efficiency with variable demand: SEC's shifting or flattening?. In: IFIP advances in information and communication technology. Springer New York LLC; 2015. p. 705–14. https://doi.org/10.1007/978-3-319-22756-6_86.
[38] Thanganadar D, Fornarelli F, Camporeale S, Asfand F, Patchigolla K. Off-design and annual performance analysis of supercritical carbon dioxide cycle with thermal storage for CSP application. Appl Energy 2021;282. https://doi.org/10.1016/j.apenergy.2020.116200.
[39] Bai Z, Yuan Y, Kong D, Zhou S, Li Q, Wang S. Potential of applying the thermochemical recuperation in combined cooling, heating and power generation: off-design operation performance. Appl Energy 2023;348. https://doi.org/10.1016/j.apenergy.2023.121523.
[40] Tiktas A, Gunerhan H, Hepbasli A, Açıkkalp E. Extended exergy analysis of a novel integrated absorptional cooling system design without utilization of generator for economical and robust provision of higher cooling demands. Energ Conver Manage 2024;307:118350. https://doi.org/10.1016/J.ENCONMAN.2024.118350.
[41] Jockenhöfer H, Steinmann W-D, Bauer D. Detailed numerical investigation of a pumped thermal energy storage with low temperature heat integration. Energy 2018;145:665–76. https://doi.org/10.1016/j.energy.2017.12.087.
[42] Zhang C, Sun J, Qiao Y, Wei J. Design, off-design and operation study of concentrating solar power system with calcium-looping thermochemical energy storage and photovoltaic-driven compressed CO2 energy storage. Energy 2024;312. https://doi.org/10.1016/j.energy.2024.133687.
[43] Morosini E, et al. Off-design of a CO2-based mixture transcritical cycle for CSP applications: analysis at part load and variable ambient temperature. Appl Therm Eng 2024;236. https://doi.org/10.1016/j.applthermaleng.2023.121735.
[44] Salah SI, Abdeldayem AS, White MT, Sayma AI. Off-design performance assessment of an axial turbine for a 100 MWe concentrated solar power plant operating with CO2 mixtures. Appl Therm Eng 2024;238. https://doi.org/10.1016/j.applthermaleng.2023.122001.
[45] Zhang C, Sun J, Qiao Y, Wei J. Design, off-design and operation study of concentrating solar power system with calcium-looping thermochemical energy storage and photovoltaic-driven compressed CO_2 energy storage. Energy 2024;312. https://doi.org/10.1016/j.energy.2024.133687.
[46] Karasavvas E, Panopoulos KD, Papadopoulou S, Voutetakis S. Energy and exergy analysis of the integration of concentrated solar power with calcium looping for power production and thermochemical energy storage. Renew Energy 2020;154:743–53. https://doi.org/10.1016/j.renene.2020.03.018.
[47] Tiktas A. Introducing a novel wind-driven passive cooling strategy for polar shelters: backed by flow dynamics and irreversibility mapping with exergy analysis. Energ Conver Manage 2025;346:120481. https://doi.org/10.1016/J.ENCONMAN.2025.120481.
[48] Salah SI, Abdeldayem AS, White MT, Sayma AI. Off-design performance assessment of an axial turbine for a 100 MWe concentrated solar power plant operating with CO_2 mixtures. Appl Therm Eng 2024;238. https://doi.org/10.1016/j.applthermaleng.2023.122001.
[49] Razmi AR, Janbaz M. Exergoeconomic assessment with reliability consideration of a green cogeneration system based on compressed air energy storage (CAES). Energ Conver Manage 2020;204. https://doi.org/10.1016/j.enconman.2019.112320.
[50] Tiktas A. Optimization-based exergoeconomic assessment of an ammonia–water geothermal power system with an elevated heat source temperature. Energies (Basel) 2025;18(19). https://doi.org/10.3390/en18195195.
[51] Yousef MS, Hassan H. Energy payback time, exergoeconomic and enviroeconomic analyses of using thermal energy storage system with a solar desalination system: an experimental study. J Clean Prod 2020;270. https://doi.org/10.1016/j.jclepro.2020.122082.
[52] Guelpa E, Capone M. Exergoeconomic analysis for the optimal exploitation of heat in thermochemical storage units integrated with concentrated solar power. 2018.
[53] P. Saini *et al.*, "Techno-economic assessment of a novel hybrid system of solar thermal and photovoltaic driven sand storage for sustainable industrial steam production," Energ Conver Manage, vol. 292, 2023, doi:https://doi.org/10.1016/j.enconman.2023.117414.
[54] Gordon JM, Fasquelle T, Nadal E, Vossier A. Providing large-scale electricity demand with photovoltaics and molten-salt storage. Renew Sustain Energy Rev 2021;135. https://doi.org/10.1016/j.rser.2020.110261.
[55] Ortiz C, Romano MC, Valverde JM, Binotti M, Chacartegui R. Process integration of calcium-looping thermochemical energy storage system in concentrating solar power plants. Energy 2018;155:535–51. https://doi.org/10.1016/j.energy.2018.04.180.
[56] Valverde JM, Medina S. Crystallographic transformation of limestone during calcination under CO_2. Phys Chem Chem Phys 2015;17(34):21912–26. https://doi.org/10.1039/c5cp02715b.
[57] Amghar N, Perejón A, Ortiz C, Pérez Maqueda LA, Sánchez-Jiménez PE. Influence of long-term CaO storage conditions on the calcium looping thermochemical reactivity. Energy Fuels 2023;37(21):16904–14. https://doi.org/10.1021/acs.energyfuels.3c02652.
[58] Valverde JM. On the negative activation energy for limestone calcination at high temperatures nearby equilibrium. Chem Eng Sci 2015;132:169–77. https://doi.org/10.1016/J.CES.2015.04.027.
[59] Peng X, Yao M, Root TW, Maravelias CT. Design and analysis of concentrating solar power plants with fixed-bed reactors for thermochemical energy storage. Appl Energy 2020;262. https://doi.org/10.1016/j.apenergy.2020.114543.
[60] Durán-Olivencia FJ, Ebri JMP, Espín MJ, Valverde JM. The cohesive behavior of granular solids at high temperature in solar energy storage. Energy Convers Manag 2021;240. https://doi.org/10.1016/j.enconman.2021.114217.
[61] Valverde JM, Sanchez-Jimenez PE, Perez-Maqueda LA. Limestone calcination nearby equilibrium: kinetics, CaO crystal structure, sintering and reactivity. J Phys Chem C 2015;119(4):1623–41. https://doi.org/10.1021/jp508745u.
[62] Ouyang T, Qin P, Xie S, Tan X, Pan M. Flexible dispatch strategy of purchasing-selling electricity for coal-fired power plant based on compressed air energy storage. Energy 2023;267. https://doi.org/10.1016/j.energy.2022.126578.
[63] Zhang W, Xue X, Liu F, Mei S. Modelling and experimental validation of advanced adiabatic compressed air energy storage with off-design heat exchanger. IET Renew Power Gener 2020;14(3):389–98. https://doi.org/10.1049/iet-rpg.2019.0652.
[64] Chen X, Jin X, Ling X, Wang Y. Exergy analysis of concentrated solar power plants with thermochemical energy storage based on calcium looping. ACS Sustain Chem Eng 2020;8(21):7928–41. https://doi.org/10.1021/acssuschemeng.0c01586.
[65] Wang Z, He N, Chen Q, Zhang Y, Yao L. Co-generation of methanol and electricity using integrated concentrated solar power, calcium looping, and methane bi-reforming: energy, exergy and economic analyses. Energy Convers Manag 2025;327. https://doi.org/10.1016/j.enconman.2025.119585.
[66] Calderón M, Calderón AJ, Ramiro A, González JF, González I. Evaluation of a hybrid photovoltaic-wind system with hydrogen storage performance using exergy analysis. Int J Hydrogen Energy 2011;36(10):5751–62. https://doi.org/10.1016/j.ijhydene.2011.02.055.
[67] Kumar R. Case based scenario questions. 2024.
[68] Schwarz JB, Andrews DN. Considerations for gas stand measurement of turbocharger performance. In: Institution of mechanical engineers - 11th international conference on turbochargers and turbocharging; 2014. p. 253–64. https://doi.org/10.1533/978081000342.253.
[69] Guisado JM, Becerra JA, Chacartegui R. Scenarios for energy recovery from slaughterhouse wastes in Europe. iScience 2025:112943. https://doi.org/10.1016/j.isci.2025.112943.
[70] Tiktas A, Gunerhan H, Hepbasli A. Single and multigeneration Rankine cycles with aspects of thermodynamical modeling, energy and exergy analyses and optimization: a key review along with novel system description figures. Energy Convers Manage X 2022;14:100199. https://doi.org/10.1016/J.ECMX.2022.100199.
[71] European Commission, "Eurostat".
[72] Bayon A, et al. Techno-economic assessment of solid–gas thermochemical energy storage systems for solar thermal power applications. Energy 2018;149:473–84. https://doi.org/10.1016/j.energy.2017.11.084.
[73] Michalski S, Hanak DP, Manovic V. Techno-economic feasibility assessment of calcium looping combustion using commercial technology appraisal tools. J Clean Prod 2019;219:540–51. https://doi.org/10.1016/j.jclepro.2019.02.049.
[74] Tiktaş A, Gunerhan H, Hepbasli A, Açıkkalp E. Exergy-based techno-economic and environmental assessments of a proposed integrated solar powered electricity generation system along with novel prioritization method and performance indices. Process Saf Environ Protect 2023;178:396–413. https://doi.org/10.1016/J.PSEP.2023.08.048.
[75] Guo H, Xu Y, Guo C, Zhang Y, Hou H, Chen H. Off-design performance of CAES systems with low-temperature thermal storage under optimized operation strategy. J Energy Storage 2019;24. https://doi.org/10.1016/j.est.2019.100787.
[76] Guisado JM, Becerra JA, Marques-Valderrama A, Chacartegui R. Solar fuels based on the integration of food wastes and photovoltaic through energy storage. Appl Energy 2026;413:127762. https://doi.org/10.1016/J.APENERGY.2026.127762.
[77] Ghorbanian K, Gholamrezaei M. An artificial neural network approach to compressor performance prediction. Appl Energy 2009;86(7–8):1210–21. https://doi.org/10.1016/j.apenergy.2008.06.006.
[78] Ortiz C, Valverde JM, Chacartegui R, Perez-Maqueda LA, Giménez P. The calcium-looping ($CaCO_3$/CaO) process for thermochemical energy storage in concentrating

solar power plants. Renew Sustain Energy Rev 2019;113. https://doi.org/10.1016/j.rser.2019.109252.
[79] Atalay H, Cankurtaran E. Energy, exergy, exergoeconomic and exergo-environmental analyses of a large scale solar dryer with PCM energy storage medium. Energy 2021;216. https://doi.org/10.1016/j.energy.2020.119221.
[80] Ehyaei MA, Rosen MA. Optimization of a triple cycle based on a solid oxide fuel cell and gas and steam cycles with a multiobjective genetic algorithm and energy, exergy and economic analyses. Energ Conver Manage 2019;180:689–708. https://doi.org/10.1016/j.enconman.2018.11.023.
[81] Wang X, Dai Y. Exergoeconomic analysis of utilizing the transcritical CO2 cycle and the ORC for a recompression supercritical CO2 cycle waste heat recovery: a comparative study. Appl Energy 2016;170:193–207. https://doi.org/10.1016/j.apenergy.2016.02.112.
[82] Chauhan A, Saini RP. Techno-economic feasibility study on integrated renewable energy system for an isolated community of India. Elsevier Ltd; 2016. https://doi.org/10.1016/j.rser.2015.12.290.
[83] "19_CHE_0924_EconInd_p45".
[84] Chauhan A, Saini RP. Techno-economic feasibility study on Integrated Renewable Energy System for an isolated community of India. Elsevier Ltd.; 2016. https://doi.org/10.1016/j.rser.2015.12.290. Jun. 01,.
[85] "19_CHE_0924_EconInd_p45".